Department of Mechanical and Aerospace Engineering

Master's Degree in Mechanical Engineering

Mistuning Identification in Bladed Disks Based on Antiresonance Frequencies

Master's Thesis

Supervisor:
Prof. Teresa M. Berruti

Candidate:
Tarik Oguz Arslan
329488

Contents

Table of Figures

Abstract

Turbomachinery is used across a wide range of applications, from energy generation to aviation. One of the main components of these machines is the rotating bladed disk. Because of their high operating speeds, bladed disks are subjected to harmonic excitation over a broad frequency range, and predicting their dynamic response accurately is a demanding part of the design process. The cyclically symmetric structure of a tuned bladed disk allows its dynamics to be analyzed at a low computational cost using a single sector. In practice, however, manufacturing tolerances and operational wear introduce small deviations between sectors that break this symmetry, a phenomenon known as mistuning. A mistuned bladed disk can localize vibration energy on a few blades and amplify their response well beyond the tuned level, which can shorten fatigue life and lead to high cycle fatigue failure. For this reason, the identification of mistuning has received considerable attention over the past few decades.

Most established identification methods map mistuning from deviations in the resonance frequencies, but their accuracy is limited by blade-disk coupling, whose effects are difficult to separate from the mistuning itself. An antiresonance-based identification method was recently introduced by Li et al. to reduce the influence of this coupling. The method draws an analogy between bladed disks and cyclic metamaterials: each blade is treated as a local resonator, so that the shift in its blade-alone frequency caused by mistuning is reflected in the antiresonance frequencies of the assembly. Because the observed antiresonance frequency depends on the location of the response measurement, a Measurement Point Correction (MPC) strategy is used to recover the true blade-alone frequency from a single, well-chosen measurement point.

This thesis implements and validates the method in a controlled finite element environment. A dummy blisk with twelve sectors and a prescribed Young's modulus mistuning pattern is built in ANSYS Mechanical, so that the ground truth is known exactly. A harmonic analysis is performed on the tuned model with detuning masses, and the node whose antiresonance frequency is closest to the blade-alone first bending frequency is selected as the measurement point. The detuning strategy is then applied to the mistuned model blade by blade, and the antiresonance frequency at the selected node of each sector is recorded. These values are converted into the Young's modulus of each blade and compared with the imposed mistuning pattern. The identified pattern reproduces the imposed one with a deviation below two percent on the most mistuned blade, confirming the accuracy of the method on a finite element model.

1. Theoretical Background on Bladed Disk Dynamics

1.1. Anatomy of Integrally Bladed Disk

Rotors are crucial components of turbomachinery used in power generation and aerospace propulsion. These structures usually operate at extremely high speeds, therefore a careful analysis for their vibratory response should be conducted. They are nominally designed in a cyclic symmetry where each sector contains a part of the disk and a single blade. This symmetry allows the dynamic response of the structure to be efficiently computed by analyzing only one sector.

Figure 1 Integrally Bladed Disk (Blisk)

In practice, however, manufacturing tolerances, material inhomogeneities, and operational wear introduce small deviations among sectors. These deviations break the cyclic symmetry and are collectively referred to as mistuning. Even in the presence of small mistuning, the forced response can be much higher than the simulations done by using the tuned mode due to modal localization and changes in energy distribution among the blades. Consequently, the identification of these variations is crucial for understanding how the system will behave in operation. In this thesis, a novel mistuning identification method based on antiresonance frequencies is investigated.

1.2. Physical Model and Equations of Motion

This section follows mainly the course material on bladed disk dynamics from the Dynamics course taught by the Aer-Mec Research Group at Politecnico di Torino [1]. A bladed disk is comprised of N identical sectors along its circumference. Since every sector has a blade and its corresponding slice of the shared disk, they all share the same geometry. This symmetry can be leveraged to efficiently model the dynamic behavior of the system.

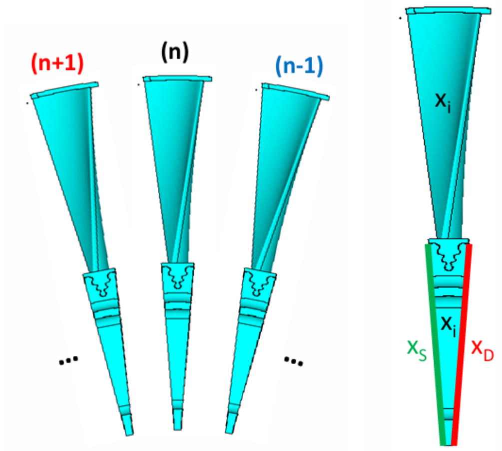

Figure 2 Fundamental sectors

The degrees of freedom of the n-th sector are partitioned into three groups: internal nodes $\mathbf{x}_{\mathrm{I}}^{(n)}$, right interface nodes $\mathbf{x}_{\mathrm{D}}^{(n)}$ shared with sector n+1, and left interface nodes $\mathbf{x}_{\mathrm{S}}^{(n)}$ shared with sector n-1. Since the left interface of a sector n coincides geometrically with the right interface of sector n+1, the DOF vector of sector n is

$$\mathbf{x}^{(n)} = \begin{bmatrix} \mathbf{x}_D^{(n)} \\ \mathbf{x}_I^{(n)} \\ \mathbf{x}_D^{(n+1)} \end{bmatrix} \tag{1.1}$$

In engineering it is common practice to start an analysis with a very basic, representative model of the whole system. As mentioned earlier, the blisks are cyclically symmetric, and each sector can be represented by lumped parameters.

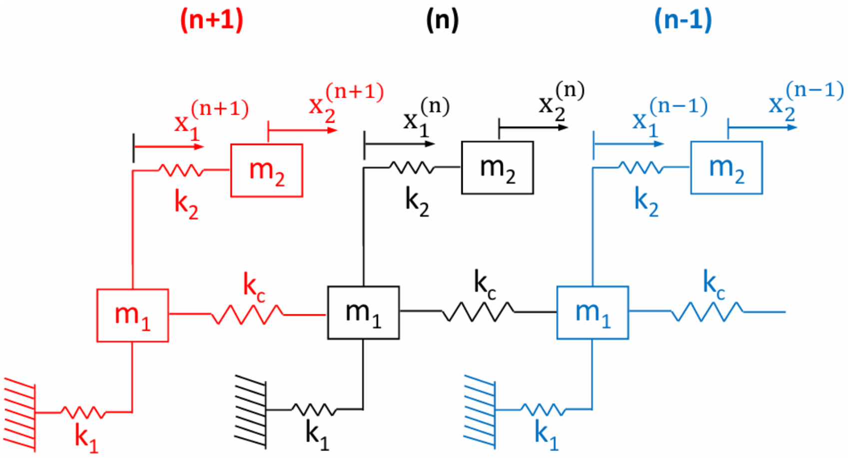

Figure 3 Rotationally Periodic Structure

The model shown in Figure 3 is a representation of cyclic symmetry with lumped parameters.

For a tuned system:

$$m_{1n} = m_1 \ \forall n \tag{1.2}$$
$$k_{1n} = k_1 \ \forall n \tag{1.3}$$
$$m_{2n} = m_2 \ \forall n \tag{1.4}$$
$$k_{2n} = k_2 \ \forall n \tag{1.5}$$

Here m_1 and m_2 are disk and blade masses in a sector, respectively. k_1 and k_2 are disk and blade stiffness coefficient in a sector, respectively. Focusing on the one sector, one can derive the equation of motions.

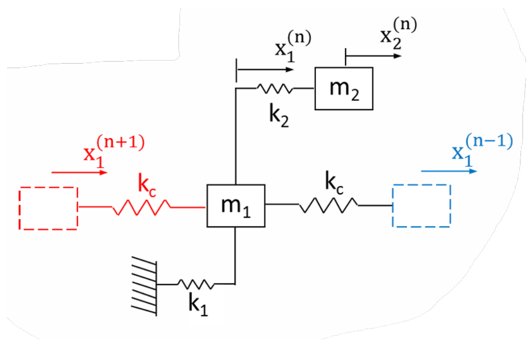

Figure 4 One sector lumped parameter approach

$$\begin{gathered} m_1\ddot{x}_1^{(n)} + k_1 x_1^{(n)} + k_2\left(x_1^{(n)} - x_2^{(n)}\right) + k_c\left(x_1^{(n)} - x_1^{(n+1)}\right) \\ + k_c\left(x_1^{(n)} - x_1^{(n-1)}\right) = 0 \end{gathered} \tag{1.6}$$

$$m_2\ddot{x}_2^{(n)} + k_2\left(x_2^{(n)} - x_1^{(n)}\right) = 0 \tag{1.7}$$

Introducing matrix notation

$$\begin{gathered} \begin{bmatrix} m_1 & 0 \\ 0 & m_2 \end{bmatrix} \begin{Bmatrix} \ddot{x}_1^{(n)} \\ \ddot{x}_2^{(n)} \end{Bmatrix} + \begin{bmatrix} k_1 + k_2 + 2k_c & -k_2 \\ -k_2 & k_2 \end{bmatrix} \begin{Bmatrix} x_1^{(n)} \\ x_2^{(n)} \end{Bmatrix} \\ + \begin{bmatrix} -k_c & 0 \\ 0 & 0 \end{bmatrix} \begin{Bmatrix} x_1^{(n+1)} \\ x_2^{(n+1)} \end{Bmatrix} + \begin{bmatrix} -k_c & 0 \\ 0 & 0 \end{bmatrix} \begin{Bmatrix} x_1^{(n-1)} \\ x_2^{(n-1)} \end{Bmatrix} = 0 \end{gathered} \tag{1.8}$$

$$\left[m^{(n)}\right]\left\{\ddot{x}^{(n)}\right\} + \left[k^{(n)}\right]\left\{x^{(n)}\right\} + \left[k_c^{(n)}\right]\left\{x^{(n+1)}\right\} + \left[k_c^{(n)}\right]\left\{x^{(n-1)}\right\} = 0 \tag{1.9}$$

Seeking harmonic solution $x^{(n)}(t) = \bar{x}^{(n)}e^{i\omega t}$ and substituting into equation (1.9), the undamped equation of sector *n* becomes

$$(-\omega^2\mathbf{m} + \mathbf{k})\mathbf{x}^{(n)} = \mathbf{0} \tag{1.10}$$

For a blisk with N number of blades, equation (1.9) can be written N times. For the equation of the first blade, the term with number of (n-1) will coincide with the sector with the number of N. Similarly, for the equation of the last sector (N), the term with number of (n+1) will coincide with the first sector. The mass matrix becomes

$$\mathbf{M} = \begin{bmatrix} m^{(1)} & 0 & \dots & 0 \\ 0 & m^{(2)} & \dots & 0 \\ \vdots & & \ddots & \vdots \\ 0 & \dots & 0 & m^{(N)} \end{bmatrix} \tag{1.11}$$

Mass matrix is block-diagonal matrix.

And the stiffness matrix can be written as

$$\mathbf{K} = \begin{bmatrix} k^{(1)} & k_c^{(1)} & 0 & & & & 0 & 0 & k_c^{(1)} \\ k_c^{(2)} & k^{(2)} & k_c^{(2)} & & & & 0 & 0 & 0 \\ 0 & k_c^{(3)} & k^{(3)} & & & & & & \\ & & & \ddots & & & & & \\ & \vdots & & k_c & k & k_c & & \vdots & \\ & & & & & \ddots & & & \\ 0 & 0 & & & & & k_c^{(N-2)} & k_c^{(N-2)} & 0 \\ 0 & 0 & & \dots & & & k_c^{(N-1)} & k_c^{(N-1)} & k_c^{(N-1)} \\ k_c^{(N)} & 0 & & & & & 0 & k_c^{(N)} & k_c^{(N)} \end{bmatrix}_{2N \times 2N} \tag{1.12}$$

Stiffness matrix is a block-circulant matrix. Note that the matrices k and k_c are identical for each sector for a tuned system. Therefore equation (1.12) becomes

$$\mathbf{K} = \begin{bmatrix} k & k_c & 0 & & & & 0 & 0 & k_c \\ k_c & k & k_c & & & & 0 & 0 & 0 \\ 0 & k_c & k & & & & & & \\ & & & \ddots & & & & & \\ & \vdots & & k_c & k & k_c & & \vdots & \\ & & & & & \ddots & & & \\ 0 & 0 & & & & & k_c & k_c & 0 \\ 0 & 0 & & \dots & & & k_c & k_c & k_c \\ k_c & 0 & & & & & 0 & k_c & k_c \end{bmatrix} \tag{1.13}$$

The top-right and bottom-left blocks in equation (1.13) represent the cyclic coupling between the first and last sector. The block-circulant structure is the foundation for the decomposition of the eigenvalue problem into N independent sector-level problems, one for each harmonic index h.

The degrees of freedom of the system can be written as

$$\ddot{\mathbf{x}} = \begin{Bmatrix} \ddot{x}^{(1)} \\ \ddot{x}^{(2)} \\ \vdots \\ \ddot{x}^{(N)} \end{Bmatrix}, \mathbf{x} = \begin{Bmatrix} x^{(1)} \\ x^{(2)} \\ \vdots \\ x^{(N)} \end{Bmatrix} \tag{1.14}$$

The final equation of motion becomes

$$\mathbf{M}\ddot{\mathbf{x}} + \mathbf{K}\mathbf{x} = \mathbf{0} \tag{1.15}$$

1.3. Modal Properties of the Tuned System

For a rotationally periodic structure, the set of valid mode shapes is invariant under a coordinate system rotation of $2\pi/N$. Considering the mode shape vector

$$\mathbf{\Phi} = \begin{Bmatrix} \Phi^{(1)} \\ \Phi^{(2)} \\ \vdots \\ \Phi^{(N-1)} \\ \Phi^{(N)} \end{Bmatrix} \tag{1.16}$$

A key symmetry property constrains the admissible mode shapes. If $\mathbf{\Phi}$ is a mode shape at natural frequency ω_n, then rotating $\mathbf{\Phi}$ rigidly by one sector angle $2\pi/N$ produces a vector $\mathbf{\Phi}'$ that is also a mode shape at the same frequency. To satisfy this rotational invariance, the structure's mode shapes will naturally fall into three categories:

a. Symmetric modes: all sectors move in the same direction with identical displacement, $\mathbf{\Phi}^{(n)} = \mathbf{\Phi}^{(n+1)}$. These are often referred to as "umbrella" modes.
b. Alternating modes: The pattern alternates in sign between adjacent sectors $\mathbf{\Phi}^{(n)} = -\mathbf{\Phi}^{(n+1)}$. Requires N to be even
c. Traveling wave modes: The displacement pattern shifts across the sectors by a constant angle, creating a pair of identical mode shapes rotated relative to each other.

Types (a) and (b) correspond to single (unrepeated) eigenvalues. Type (c) modes always appear in degenerate pairs sharing the same natural frequency.

1.3.1. Double Multiplicity and the Inter-Sector Phase Relation

Let $\mathbf{\Phi}$ and $\widehat{\mathbf{\Phi}}$ be two orthonormal eigenvectors at the same frequency ω_n. The rotated vector $\mathbf{\Phi}'$ must lie in the same eigenspace, so

$$\mathbf{\Phi}' = c\mathbf{\Phi} + s\,\widehat{\mathbf{\Phi}} \tag{1.17}$$

Enforcing normalization shows that $c = cos\varphi$ and $s = sin\varphi$, giving the sector-to-sector rotation

$$\begin{bmatrix} \mathbf{\Phi}^{(n-1)} \\ \widehat{\mathbf{\Phi}}^{(n-1)} \end{bmatrix} = \begin{bmatrix} \mathbf{I}_J \cos\varphi & \mathbf{I}_J \sin\varphi \\ -\mathbf{I}_J \sin\varphi & \mathbf{I}_J \cos\varphi \end{bmatrix} \begin{bmatrix} \mathbf{\Phi}^{(n)} \\ \widehat{\mathbf{\Phi}}^{(n)} \end{bmatrix} \tag{1.18}$$

Any linear combination of $\mathbf{\Phi}$ and $\widehat{\mathbf{\Phi}}$ is a valid eigenvector at ω_n, confirming the double multiplicity of type (c) modes.

1.3.2. Complex Modes and Traveling Waves

It is more transparent to work with two complex eigenvectors formed from the real pair

$$\overline{\mathbf{\Theta}}^{+} = \mathbf{\Phi} + i\widehat{\mathbf{\Phi}}, \qquad \overline{\mathbf{\Theta}}^{-} = \mathbf{\Phi} - i\widehat{\mathbf{\Phi}} \tag{1.19}$$

The rotation relation written in equation (1.18) the simplifies to a multiplicative phase shift between adjacent sectors

$$\overline{\mathbf{\Theta}}^{+(n)} = \overline{\mathbf{\Theta}}^{+(n-1)} e^{-i\varphi}, \qquad \overline{\mathbf{\Theta}}^{-(n)} = \overline{\mathbf{\Theta}}^{-(n-1)} e^{+i\varphi} \tag{1.20}$$

Each sector vibrates with the same modal shape as its neighbor, advanced or delayed by φ. The response associated with $\overline{\mathbf{\Theta}}^{+}$ is a forward-traveling wave sweeping around the disk, $\overline{\mathbf{\Theta}}^{-}$ is the corresponding backward-traveling wave. Their superposition recovers the real standing-wave pair $(\mathbf{\Phi}, \widehat{\mathbf{\Phi}})$.

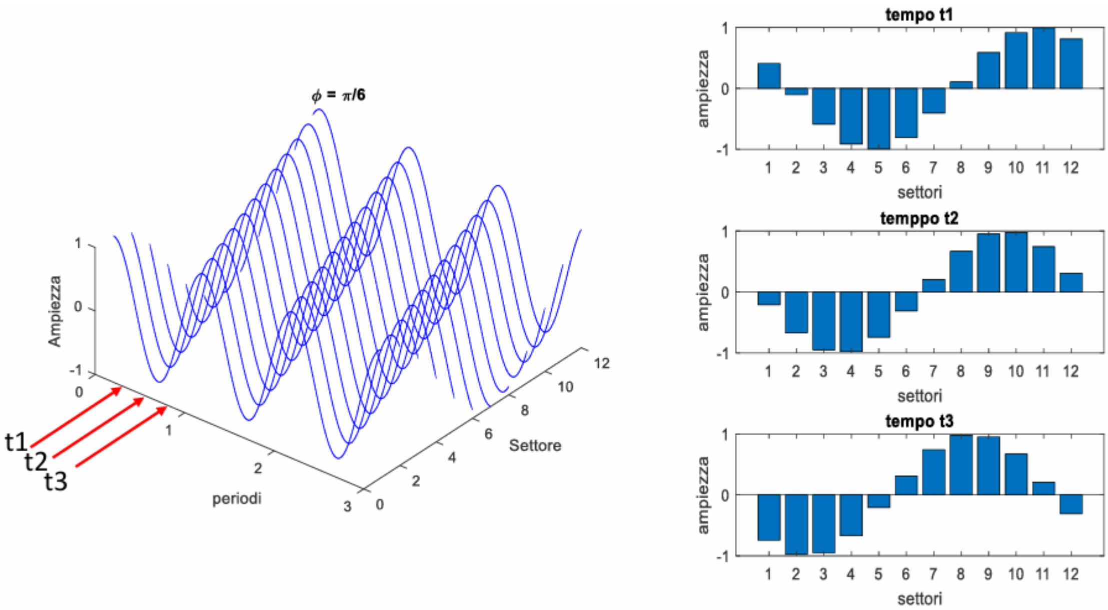

Figure 5 Wave representation

1.3.3. Admissible Harmonic Indices and Nodal Diameters

For a traveling wave to repeat itself after completing one full revolution, the accumulated phase shift across all N sectors must equal an integer multiple of 2π. This condition determines the inter-blade phase angle.

$$\varphi = h\frac{2\pi}{N}, \qquad h \in \mathbb{Z} \tag{1.21}$$

where h is the harmonic index. Since $e^{i\varphi}$ is 2π-periodic, values with $|h| > N/2$ correspond to phase shifts that are already represented by existing indices. Therefore, the full set of unique admissible values is

$$h \in \begin{cases} \left\{-\frac{N}{2}+1, \dots, 0, \dots, \frac{N}{2}\right\}, & N \text{ even} \\ \left\{-\frac{N-1}{2}, \dots, 0, \dots, \frac{N-1}{2}\right\}, & N \text{ odd} \end{cases} \tag{1.22}$$

The displacement of DOF j in sector n varies as

$$A_j \cos\left(2\pi h \frac{n}{N} + \delta_j\right) \tag{1.23}$$

producing exactly h diametrical lines of zero displacement, which are universally referred to as the nodal diameters.

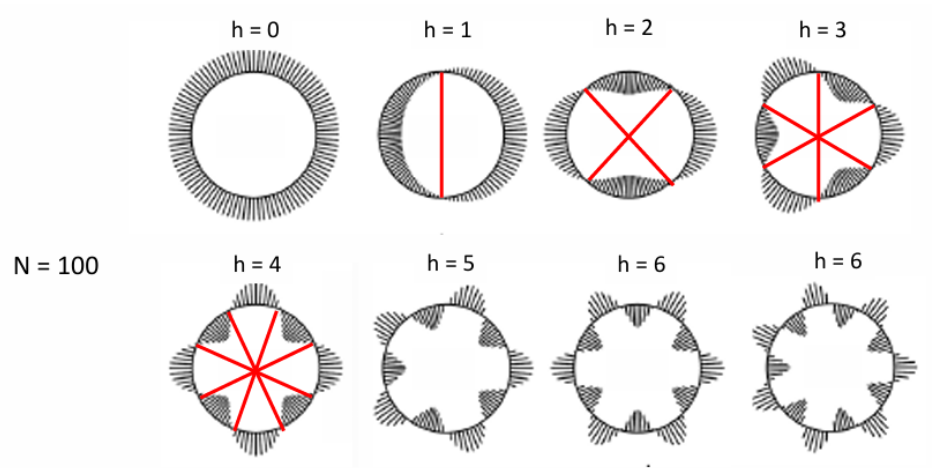

Figure 6 Representation of nodal diameters

1.4. Reduction to the Fundamental Sector

1.4.1. Transformation Matrix and Reduced Eigenvalue Problem

Equation (1.20) means the right-interface DOFs of sector n+1 are those of sector n multiplied by $e^{ih2\pi/N}$

$$\mathbf{x}_D^{(n+1)} = \mathbf{x}_D^{(n)} e^{\frac{ih2\pi}{N}} \tag{1.24}$$

This allows the full DOF vector to be written in terms of the reduced set $\bar{\mathbf{x}}_{SC}^{(n)} = \left\{\mathbf{x}_D^{(n)}, \mathbf{x}_I^{(n)}\right\}^T$ via the transformation matrix $\bar{\mathbf{T}}$

$$\mathbf{x}^{(n)} = \bar{\mathbf{T}}\bar{\mathbf{x}}_{SC}^{(n)}, \qquad \bar{\mathbf{T}} = \begin{bmatrix} \mathbf{I}_D & \mathbf{0} \\ \mathbf{0} & \mathbf{I}_I \\ \mathbf{I}_D e^{\frac{ih2\pi}{N}} & \mathbf{0} \end{bmatrix} \tag{1.25}$$

Substituting into equation (1.10) and pre-multiplying by $\bar{\mathbf{T}}^T$ gives the reduced eigenvalue problem for the fundamental sector

$$\left(-\omega^2 \mathbf{m}_{SC}^{(h)} + \mathbf{k}_{SC}^{(h)}\right)\bar{\mathbf{x}}_{SC}^{(n)} = \mathbf{0} \tag{1.26}$$

With $\mathbf{m}_{SC}^{(h)} = \bar{\mathbf{T}}^T\mathbf{m}\bar{\mathbf{T}}$ and $\mathbf{k}_{SC}^{(h)} = \bar{\mathbf{T}}^T\mathbf{k}\bar{\mathbf{T}}$. Solving equation (1.26) for each admissible h yields the natural frequencies and fundamental-sector mode shapes, the full disk mode shape follows from equation (1.20). Instead of one problem of size *NJ*, only [*N*/2]+1 problems of size *J* need to be solved.

1.4.2. Natural Frequency Diagram

Plotting the calculated natural frequencies against the harmonic index *h* produces the frequency versus nodal diameter diagram. Each connected branch in this diagram is obtained by tracking the r-th natural frequency across all values of *h*, and this branch represents a modal family.

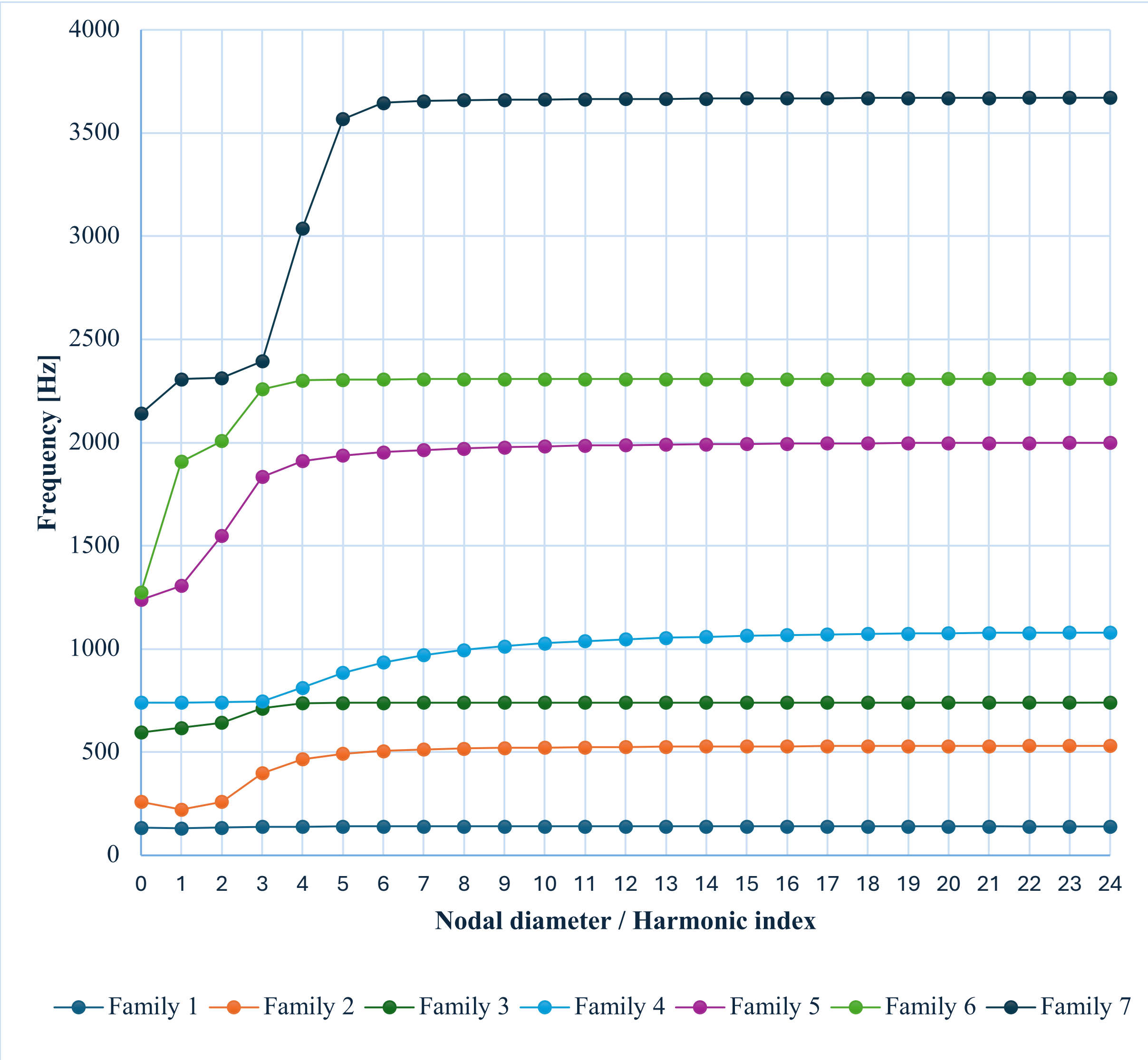

Figure 7 Frequency-nodal diameter plot of a tuned blisk

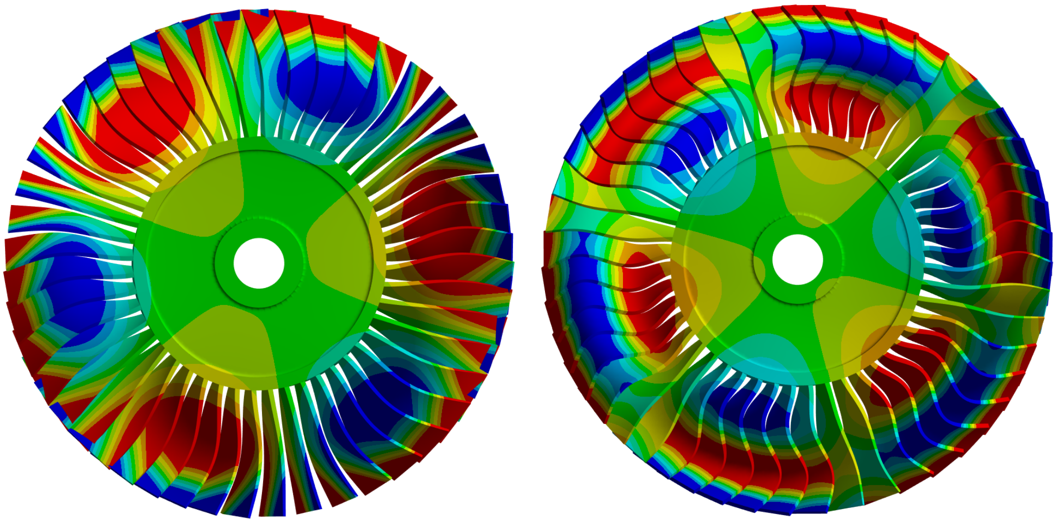

Figure 8 Two mode shapes with harmonic index h=3, Family 3 (a), and Family 5(b)

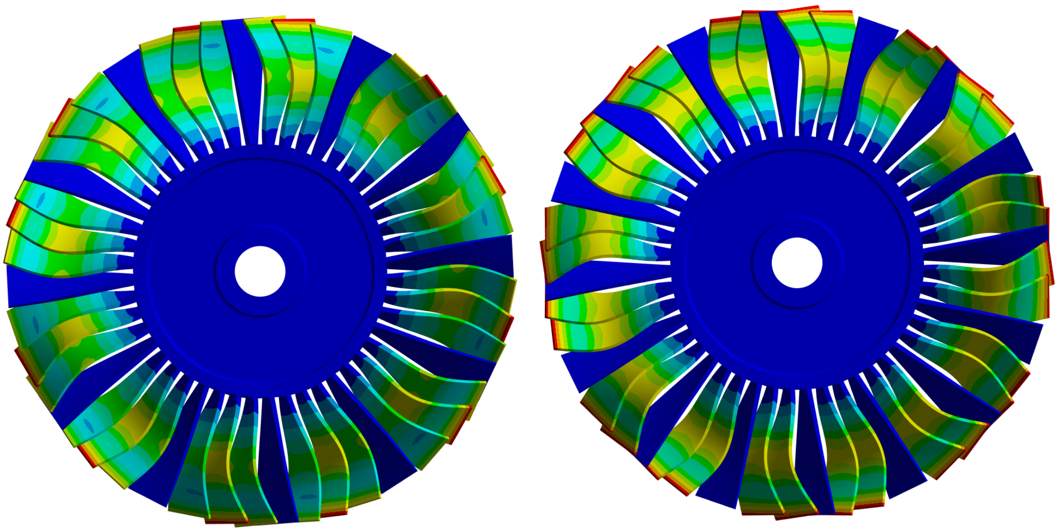

Figure 9 Two mode shapes for Family 4, h=6 (a), and h=8(b)

1.5. Forced Response and Resonance Conditions

1.5.1. Aerodynamic Forcing and Engine Order

As the integrally bladed rotor turns at rotational speed Ω, each sector passes periodically through the non-uniform aerodynamic pressure field generated by the upstream stator vanes. This aerodynamic force is periodic in the rotation angle $\alpha = \Omega t$ and can be expanded as a Fourier series. Each harmonic is characterized by its engine order (eo) with a corresponding forcing frequency of $\omega = eo \cdot \Omega$. Engine order defines the number of pressure peaks per single revolution.

Since adjacent sectors pass through the identical pressure field with a physical time delay of $\Delta t = \frac{2\pi}{N\Omega}$, the resulting force acting on sector *n*+1 lags the force on sector *n* by the phase angle

$$\psi = \mathrm{eo} \cdot \frac{2\pi}{N} \tag{1.27}$$

In complex notation the global force vector for engine order eo is

$$\mathbf{F}_{eo} = \begin{bmatrix} \mathbf{I}_J \\ \mathbf{I}_J e^{-i\psi} \\ \vdots \\ \mathbf{I}_J e^{-i(N-1)\psi} \end{bmatrix} \tag{1.28}$$

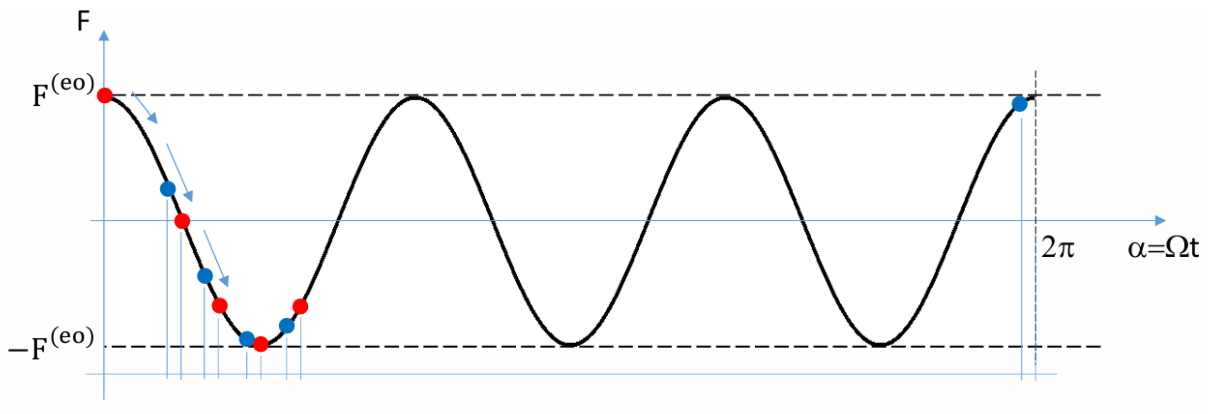

Figure 10 The red dot indicates the position of sector n, while the blue dot indicates that of sector n+1. Sector n+1 will be in the same angular position as sector n after a delay Δt

1.5.2. The Selection Rule

In modal coordinates, the amplitude of mode *r* is

$$\bar{q}_r = \frac{\bar{f}_r}{\omega_r^2 - \omega^2 + i\omega c_r}, \qquad \bar{f}_r = \mathbf{\Phi}_r^T \mathbf{F}_{\mathrm{eo}} \tag{1.29}$$

Resonance requires both $\omega = \omega_r$ and $\bar{f}_r \neq= 0$. For a mode of harmonic index h, the modal force projection reduces to

$$\bar{f}_r \propto \sum_{n=0}^{N-1} e^{in(h-\mathrm{eo})2\pi/N} \tag{1.30}$$

This sum equals *N* when $h = \mathrm{eo}$ and is zero otherwise. The necessary and sufficient conditions for resonance are

$$\boxed{\omega = \omega_r^{(h)} \;\; and \;\; h = \mathrm{eo} - kN, \qquad k \in \mathbb{Z}} \tag{1.31}$$

Engine order eo excites only those modes satisfying $h \equiv eo \ (mod\ N)$. As a consequence, many crossings that appear in the Campbell diagram are not genuine resonances.

1.5.3. Campbell Diagram and Zig-Zag Diagram

The Campbell diagram plots natural frequencies and forcing frequencies $\omega = \mathrm{eo} \cdot \Omega$ against rotational speed. Only intersections that satisfy selection rule (1.31) are genuine resonances.

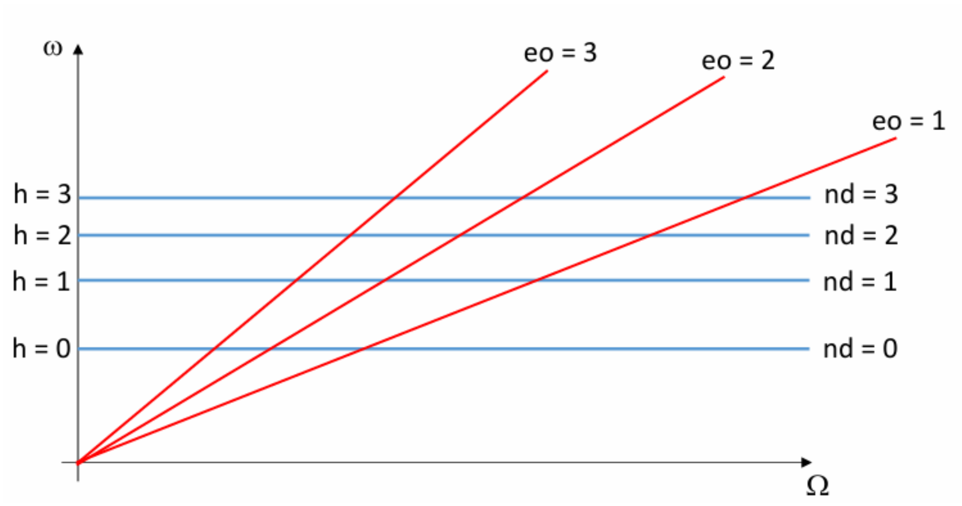

Figure 11 Campbell diagram

For engine orders larger than N, the selection rule must be evaluated using the periodicity of e^{ix}. A convenient graphical representation is provided by the zig-zag diagram (Figure 12 and Figure 13), where the harmonic index h is plotted on the horizontal axis and the engine order eo on the vertical axis. The lines defined by eo $= h + kN$ are drawn with a 45° slope, allowing the excited harmonic index corresponding to a given eo to be identified directly from the diagram. For even values of N, the negative-h branches are folded into the first quadrant because h and -h correspond to the same natural frequency.

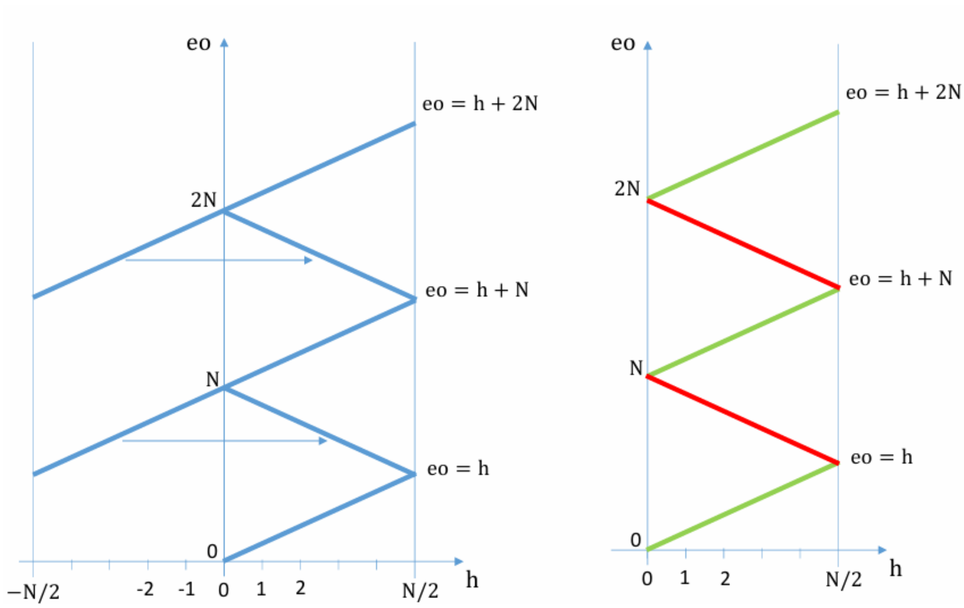

Figure 12 Zig-zag diagram with even N

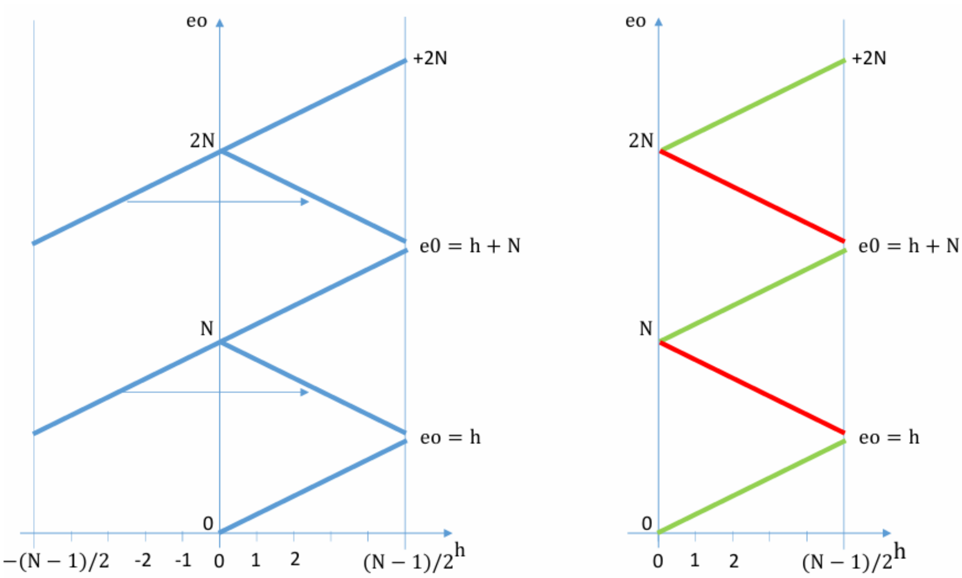

Figure 13 Zig-zag diagram with odd N

As a worked example, for N=40 and eo=37: $h = 37 - 1 \times 40 = -3$

So eo=37 excites only with $h = -3$ (three nodal diameters, backward-traveling wave). Every other crossing of the eo=37 line in the Campbell diagram is false.

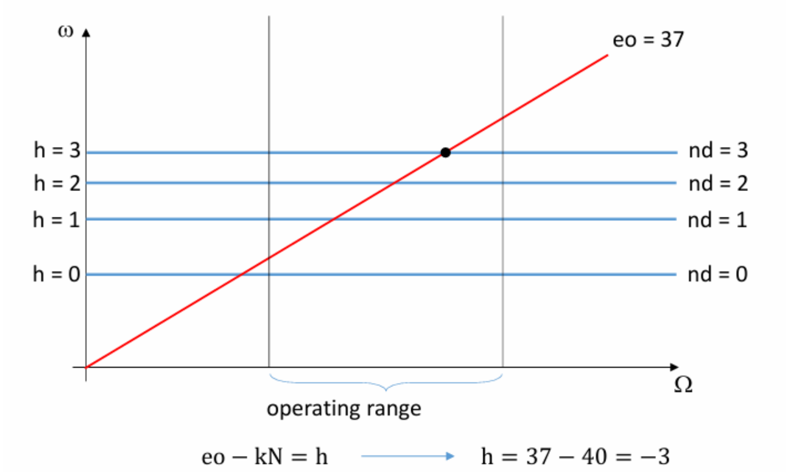

Figure 14 Example of finding critical speed

1.6. Effect of Mistuning on Dynamic Behavior

1.6.1. Definition and Sources of Mistuning

The procedures discussed thus far have assumed a tuned system composed of identical sectors. However, in reality, factors such as manufacturing tolerances and operational wear cause perturbations from nominal properties. In turbomachinery literature, these perturbations are referred to as mistuning. Mistuning can be classified into small and large categories. Small mistuning is inherently present from the very beginning of a component's operational life and is a primary concern during the design phase. Large mistuning, conversely, is often caused by more severe situations, such as the loss of one or more blades or significant damage during operation.

Because small mistuning does not change the modal shape of an individual blade in a first approximation, its presence is captured by the variability of the blade natural frequencies, blades that would be identical in a tuned system instead exhibit slightly different natural frequencies when mistuned. It is therefore natural to represent small mistuning through a perturbation of the Young's modulus of each sector, since the stiffness matrix of a component is linearly proportional to its elastic modulus. For the n-th sector, the stiffness matrix under mistuning can be written as

$$\mathbf{k}^{(n)} = (1 + \delta_n)\mathbf{k}_0 \tag{1.32}$$

Where $\mathbf{k}_0$ is the nominal tuned sector stiffness matrix which can be seen in equation (1.12) and $\delta_n \ll 1$ is the dimensionless mistuning parameter of sector n. The mistuning parameter is directly related to the deviation of the Young's modulus from its nominal value E_0

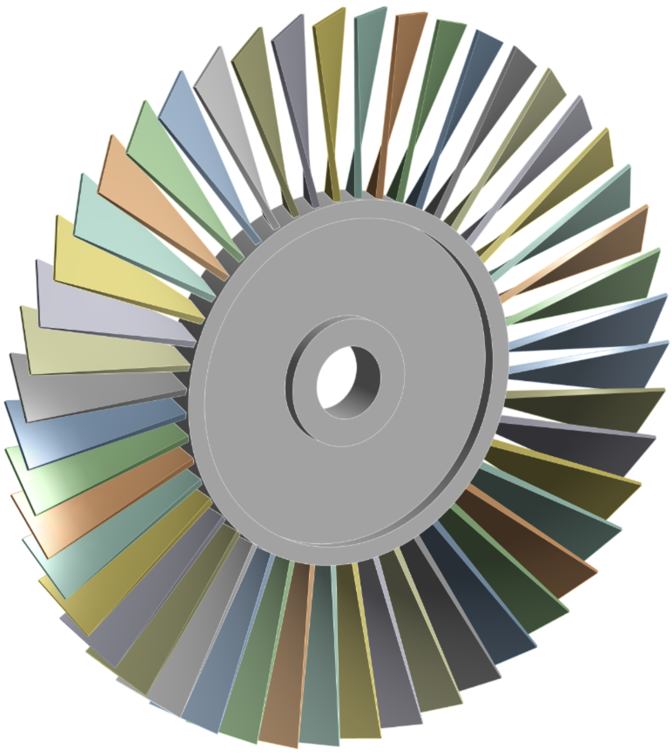

Figure 15 Blisk model with blades having different values of elastic modulus

$$\delta_n = \frac{\Delta E^{(n)}}{E_0} \tag{1.33}$$

1.6.2. Equations of Motion of the Mistuned System

The global equations of motion of the bladed disk take the same form as the tuned system,

$$\mathbf{M}\ddot{\mathbf{x}} + \mathbf{K}\mathbf{x} = \mathbf{0} \tag{1.34}$$

But the mass matrix $\mathbf{M}$ and stiffness matrix $\mathbf{K}$ now differ from their tuned counterparts. They can be decomposed as

$$\mathbf{M} = \mathbf{M}_0 + \Delta\mathbf{M}, \qquad \mathbf{K} = \mathbf{K}_0 + \Delta\mathbf{K} \tag{1.35}$$

Where $\mathbf{M}_0$ and $\mathbf{K}_0$ are the tuned system matrices, and $\Delta\mathbf{M}$ and $\Delta\mathbf{K}$ are perturbation matrices carrying the mistuning information. For stiffness mistuning only, $\Delta\mathbf{M} = \mathbf{0}$ and the perturbation matrix $\Delta\mathbf{K}$ is block-diagonal

$$\Delta\mathbf{K} = \mathrm{diag}(\delta_1\mathbf{k}_0, \delta_2\mathbf{k}_0, \dots, \delta_N\mathbf{k}_0) \tag{1.36}$$

The off-diagonal coupling blocks vanish because mistuning in the blades does not directly perturb the coupling stiffness between adjacent sectors. This structure is significant, because it shows that the perturbation matrix is entirely characterized by the N scalar parameters $\{\delta_n\}$.

1.6.3. Consequences of Mistuning: Frequency Splitting and Mode Localization

Three main consequences arise from the inclusion of mistuning in the system. They will be discussed shortly in this section. The first effect is about the natural frequencies of the model. In a tuned system, a pair of identical natural frequencies are present apart from the harmonic indices of h=0 and h=N/2. Mistuning changes this pairing by disrupting cyclic symmetry. These separated values can be measured experimentally and are among the clearest indicators of mistuning. A modal analysis of mistuned blisk with 48 blades shown in Figure 15 has been performed by using ANSYS, and the frequencies for the first family of modes are listed below. The frequency change between the first and the 48th mode is around 6.9%.

Table 1 Natural frequencies for the first family modes for mistuned system

Mode	Frequency [Hz]	Mode	Frequency [Hz]	Mode	Frequency [Hz]	Mode	Frequency [Hz]
1	132.16	13	140.84	25	141.01	37	141.11
2	132.17	14	140.87	26	141.02	38	141.11
3	135.13	15	140.9	27	141.02	39	141.12
4	135.37	16	140.9	28	141.02	40	141.12
5	135.38	17	140.93	29	141.04	41	141.14
6	139.64	18	140.93	30	141.04	42	141.14
7	139.65	19	140.96	31	141.05	43	141.14
8	140.46	20	140.97	32	141.07	44	141.15
9	140.46	21	140.98	33	141.07	45	141.15
10	140.73	22	140.98	34	141.09	46	141.18
11	140.74	23	140.99	35	141.09	47	141.18
12	140.84	24	140.99	36	141.11	48	141.19

The second main consequence is the change in mode shapes. As discussed in Section 1.3, the mode shapes of a tuned system show clear lines of no displacement, which are called nodal diameters. On the other hand, these spatial patterns do not occur when mistuning is introduced. New mode shapes contain contributions from multiple harmonic indices. For large mistuning values, the number of harmonic indices present in one modal shape increases further. An example of two different modal shapes of a blisk with small mistuning shown in Figure 16. It can be seen that the clear pattern of nodal diameters is no longer present, and localized displacements are dominant.

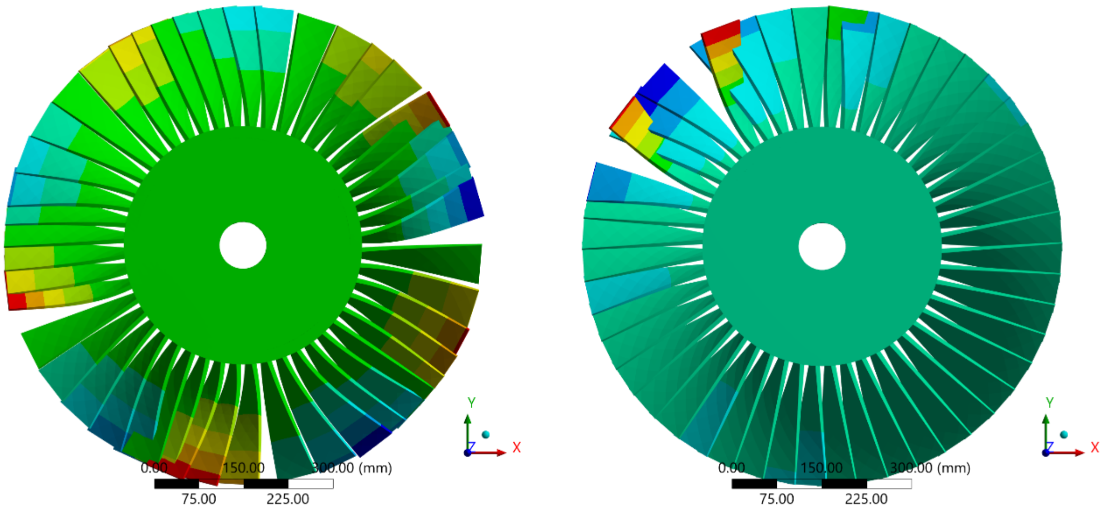

Figure 16 Modal shapes of mode 10 and 24 of mistuned blisk

The last and possibly the most important concern is the forced response localization phenomenon. When a harmonic load excites the system, a perfectly tuned one distributes the incoming vibrational energy across all sectors evenly. However, in a case with even minor mistuning present, this vibrational energy tends to localize, this results in one part of the system having much higher stress and displacement than the others. In extreme cases, this localization may occur only on one blade which can have catastrophic consequences in practice. Besides, since operational speeds can reach extreme values in gas turbine blisks, the localized amplification causes high-cycle fatigue failures. As a consequence, the identification of mistuning in blisks has utmost importance in turbomachinery literature, and a novel method for this purpose will be discussed in Chapter 3.

2. Literature Review on Mistuning

Turbomachinery bladed disks are nominally designed to possess perfect cyclic symmetry. In reality, manufacturing tolerances, material deviations, and operational wear introduce small, random variations in the structural properties of individual blades ([2]). This phenomenon is universally referred to as mistuning. While these variations are typically on the order of just a few percent, they disrupt the cyclic symmetry of the rotor and can cause mode localization. When vibrational energy becomes heavily confined to a small region or even a single blade, the forced response amplitudes and stresses drastically increase. This localized amplification acts as a primary driver for premature high cycle fatigue failures in gas turbine engines ([2]). To accurately predict and mitigate these dangerous stress magnifications, researchers must first be able to identify the mistuning parameters present in an actual manufactured rotor.

2.1. Modeling Approaches

Throughout studies on mistuning, one of the main goals of researchers was to develop efficient models of mistuned bladed disks. As discussed in Chapter 1, it is possible to accurately model a tuned, nominal blisk using lumped parameters and cyclic symmetry. However, introducing mistuning not only destroys the cyclic symmetry but also makes it extremely difficult to determine the correct lumped parameters ([3]). Besides, complete FEA of mistuned blisks was time-consuming in the early days. Therefore, new modeling techniques with accuracy close to that of finite element models and rapidity close to that of the lumped parameter approach were tried to construct. They are mainly called reduced-order modeling techniques, and in this section, some of the important studies will be briefly discussed.

Reduced-order modeling (ROM) techniques essentially divide the whole system into substructures to analyze vibrational response, see Figure 17. Castanier et al. ([4]) began with a finite element model of a sector of a tuned blisk and split it into two components: a disk portion and a blade. In their method, the mode shapes of the disk were calculated using massless blades at their interfaces, and the blade mode shapes were calculated by fixing the blade roots. The summation of the modes of these substructures allows them to build a model with fewer degrees of freedom. They reduced the DOF from 360 to 9 in one sector, achieving good accuracy over a broad range of frequencies. Yang and Griffin ([5]) also used a similar approach, but they handled the disk-blade boundaries differently, using rigid-body type translation and rotations. They applied a modified version of the receptance method to complete the mathematical model. In the end, they could construct an accurate $6N$-DOF model for each blade for a blisk with N blades. Both studies yield simple enough models to run Monte-Carlo simulations many times in a short time using component mode synthesis (CMS). Bladh et al. ([3]) developed a method of CMS, which they used the Craig-Bampton method ([6]) systematically. They introduced the secondary modal analysis reduction technique (SMART), which performs mistuning analysis in the low-order modal domain and produces results very quickly.

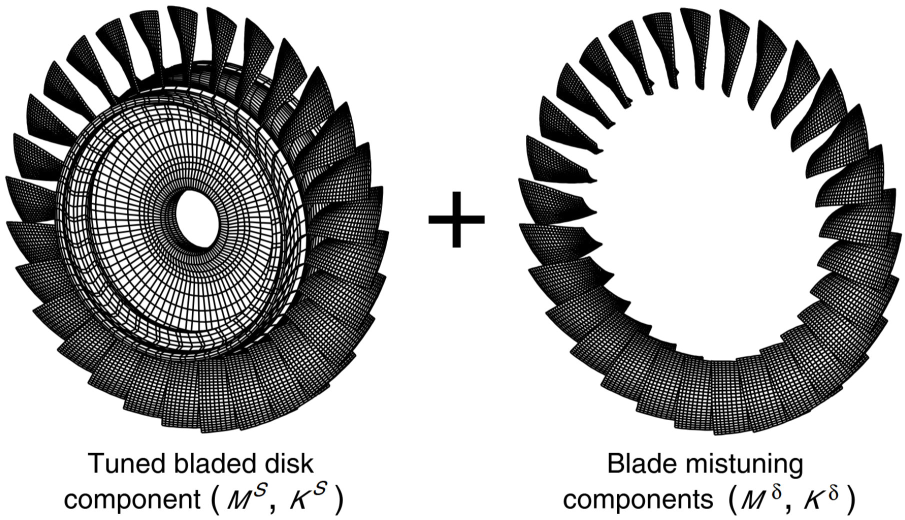

Figure 17 Substructuring for a mistuned blisk ([7])

In 2001, Yang and Griffin ([8]) published a paper introducing a different approach. Instead of modeling with substructures, they adopted nominal modes to describe the behavior of the mistuned system. In fact, their description shows that nominal modes with similar natural frequencies can successfully simulate mistuned modes in the same frequency range. Therefore, a subset of nominal modes is sufficient to represent the mistuned system modes, and they referred to this strategy as SNM. The SNM method also allowed researchers to include mistuning as a weighted sum of the tuned modes. Feiner and Griffin further simplified this approach with their fundamental mistuning model (FMM) ([9]). Using FMM, two parameter sets are enough to predict the mistuned modes and natural frequencies of the blisks: a set of nominal frequencies of the tuned system, and a set of deviations of the individual blade frequencies from their tuned value. If also the engine order of the excitation and the modal damping values are added, the flutter analysis of the system can be performed accurately. The limitation of this method is that it cannot yield accurate results when a mode lies in an area of uncertainty. These regions can be veering regions or high slope regions on the frequency versus nodal diameter plot. A method proposed by Lim et al., on the other hand, does not have difficulty dealing with these regions ([7]). The component mode mistuning (CMM) method is particularly useful here because it can systematically account for all eigenvalue mistuning patterns associated with the dominant cantilevered-blade modes interacting in that narrow frequency band. The CMM method is also highly effective for modeling nonproportional mistuning, and it can simulate highly localized vibrational responses.

Among the previously mentioned studies, only a few were able to include not only blade mistuning but also disk or sector mistuning. In 2011, Vargiu et al. ([10]) extended the CMM method in order to include sector mistuning effects. Their method, Integral Mode Mistuning (IMM), captured also the mistuning between the blades and the host disk. IMM accurately calculated the maximum forced-response amplifications at high engine-order excitations. A different strategy was pursued by Petrov et al. ([11]), who avoided modal approximation entirely by establishing an exact relationship between the forced response of the tuned and mistuned assemblies. Using the Sherman-Morrison-Woodbury identity, they expressed the mistuned response in terms of the tuned FRF matrix, allowing the model to be condensed to only the degrees of freedom where mistuning is applied, or response is of interest, without any loss of accuracy. More recently, Willeke et al. ([12]) extended a substructure-based ROM to account for rotation, capturing the stress stiffening and spin softening that shift the natural frequencies and mode shapes at operating speed. By utilizing different types of reduction techniques with mode samples at several rotational speeds, they predicted the forced response of mistuned blisks while saving about ninety percent of the computational time compared to full finite element analysis.

The methods reviewed above show how researchers gradually built models that keep the accuracy of finite element analysis but stay cheap enough to run many times over. Each approach, whether based on substructuring, modal truncation, or an exact reformulation, was aimed at the same goal: predicting the forced response of a mistuned blisk quickly, provided its mistuning pattern is already known. However, the mistuning parameters are not known beforehand to apply these techniques accurately and identifying them is another big hurdle before the use of bladed disks. In this thesis, a reduced-order model is not required, since the dummy blisk under study (Chapter 4) is simple enough to be simulated directly with a full finite element model. The main focus instead lies on the inverse problem. In the next section, different studies on the identification of mistuning are discussed.

2.2. Mistuning Identification Studies

The modeling techniques reviewed in Section 2.1 all assume that the mistuning pattern is already known. In practice it is hidden inside the finished component and must be recovered from measurements before any forced-response prediction can be made ([2]). This inverse problem has received as much attention as the modeling problem itself, and the studies discussed here approach it from several directions: from the system modes, from the as-measured blade geometry, from dedicated experiments on individual blades, and most recently from operating-condition data and machine-learning surrogates.

The earliest methods exploited the strong sensitivity of the system modes to small mistuning. Feiner and Griffin ([13]) built on this idea in 2004 with the Fundamental Mistuning Model for identification (FMM ID). Because the mistuned modes of an isolated family change markedly even for tiny frequency deviations, the modes themselves provide an accurate basis for identification, and the method requires only the tuned system frequencies and the measured mistuned modes, bypassing the full mass and stiffness matrices. In a companion study on compressor stages ([14]), they showed that an advanced version can even extract the tuned frequencies directly from the experimental data. Their measurements also revealed that the mistuning of blisks is not always random. They predicted that the mistuning on their model is caused by the tool wear while manufacturing.

Representing mistuning purely as frequency deviations is, however, a simplification, since the real source is the variation of blade geometry and material properties. To capture this more accurately, Bhartiya and Sinha ([15]) proposed in 2014 a method based on Modified Modal Domain Analysis (MMDA) with Proper Orthogonal Decomposition (POD), using coordinate-measuring-machine data to define the geometric perturbation of each blade explicitly. Beck et al. ([16]) extended this approach with a geometric mistuning reduced-order model. They scanned the rotor with optical scanners and used a mesh-metamorphosis algorithm to fit the finite element nodes to the as-measured geometry. This lets them tell apart the frequency shifts caused by geometry and those caused by material properties.

A second family of methods identifies mistuning through dedicated experiments. The classical strategy is mass detuning, in which small masses are added to every blade except one so that the natural frequency of the remaining blade can be measured. As Lupini et al. ([17]) pointed out in 2021, a single blade can never be completely isolated, since residual coupling through the disk and between neighboring blades always remains. They introduced influence coefficients to quantify it and fold it into the identification. Cimpuieru et al. ([18]) refined this by removing the unidentified cyclic modeling error of the earlier formulation and allowing the mistuning to be identified directly, without arbitrary reference values. Li et al. ([19]) approached the same coupling problem differently. They treated the blisk as a cyclic metamaterial, with each blade acting as a local resonator, and showed that the blade-alone frequencies appear as antiresonances in the disk response. An antiresonance dip is easier to locate than a cluster of resonance peaks, and it is far less sensitive to damping. Their Measurement Point Correction strategy then removes the blade–disk coupling error without any complex modeling. This thesis builds directly on their framework, which is developed in Chapter 3.

The methods above rely on stationary tests, which cannot reproduce centrifugal stiffening and Coriolis forces. Recent work has therefore moved toward identification under operating conditions. Wei et al. ([20]) combined Proper Orthogonal Modes with blade-tip-timing data to identify mistuning in a rotating blisk. Long and Chen ([21]) addressed the varying-speed case. They built a variable-speed reduced-order model (VSROM) by writing the stiffness matrix as a polynomial in rotational speed. From this model, they derived a response-based identification method that works at any speed, whether constant or variable. It needs only the measured nodal displacements, which lowers the experimental demand. In parallel, the cost of repeated analyses has driven the adoption of machine-learning models. Liang et al. ([22]) proposed a deep neural network (MS-DNN) that bypasses the physical equations. Instead of solving the coupled system, they decoupled the mistuning parameters and used neural networks to replace the coupling process, mapping the mistuning of each blade directly to the predicted response.

Taken together, these studies trace a clear evolution, from frequency-based models needing only a few modal parameters, through geometry-based and experimental techniques, to recent data-driven frameworks. A common difficulty runs through all of them: the blade-disk coupling provided by the shared disk, which prevents any blade from being measured in true isolation and which most methods must model explicitly or correct for. The antiresonance-based approach addresses this difficulty at its root, by exploiting a feature of the response that is intrinsically local to the blade and largely insensitive to coupling and damping. The remainder of this thesis develops that approach and validates it on a controlled finite element model.

3. The Antiresonance-Based Identification Method

3.1. Locally Resonant Metamaterial Analogy

Metamaterials are specifically engineered materials that can have unusual properties ([23], [24]). Advancements in metamaterials enable the development of engineered structures with unconventional dynamic properties not found in natural materials.

Previous researchers were able to create materials with a negative refractive index ([25], [26]) or auxetic materials with a negative Poisson's ratio ([27]). Mechanical metamaterials consist of periodically placed micro-scale structures that can be adjusted to have desired unusual properties. These structures, called unit cells, determine the properties of the metamaterial. Blisks share a fundamental trait with cyclic metamaterials: spatial periodicity.

In this analogy, the shared disk of the blisk can be described as a host structure, and each blade acts as a "local resonator" (LR) mounted to it. Because of this periodic arrangement of resonators on a host, the structure generates frequency band gaps. A band gap is a specific range of frequencies where vibrations are strictly forbidden from propagating through the material. In a tuned blisk, every blade is identical, meaning the band gap is uniform around the entire circumference of the blisk. However, the introduction of structural mistuning breaks this cyclic symmetry, varying the local blade properties and transforming the blisk into a 'rainbow metamaterial' ([28]). In physics, a rainbow metamaterial features a spatial grading of band gaps. Just as a glass prism disperses white light into a localized spectrum of colors, a mistuned blisk causes different sectors of the disk to trap and localize elastic waves of varying frequencies. In literature, rainbow metamaterials are primarily used to fabricate a unique material with peculiar properties. On the other hand, using this analogy, it is possible to reverse-engineer the properties of the blisk by inspecting the band gaps of the local resonators. This reverse-engineering process is the core principle used in this work for identifying mistuning in blisks.

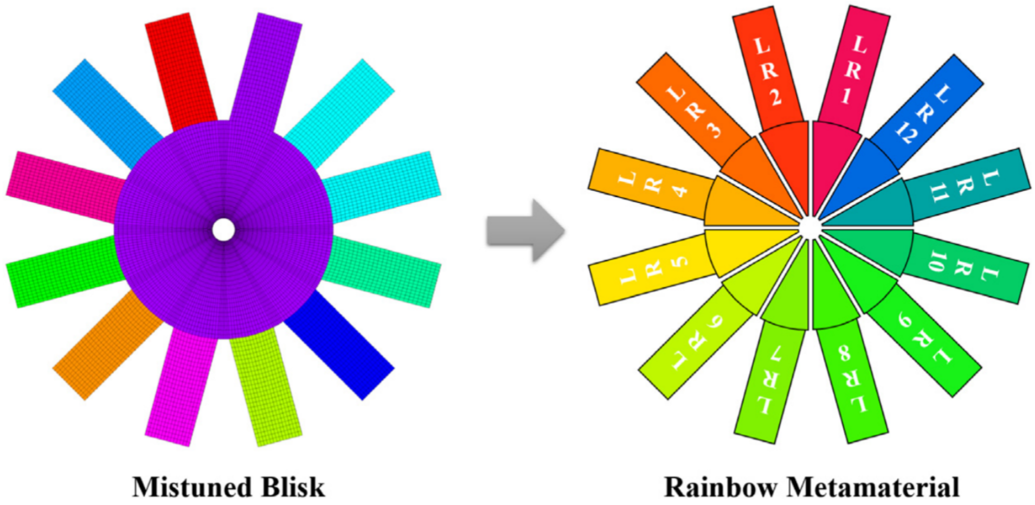

Figure 18 Representation of mistuned blisk as a rainbow metamateial ([19])

To demonstrate these wave propagation characteristics analytically, a simplified lumped mass model will be utilized. In this theoretical framework, a single sector of the blisk is treated as a unit cell. The cell consists of a mass representing the structural degree of freedom of the disk m_a connected by a stiffness element k_a representing inter-sector stiffness, alongside a branching mass-spring system (m_b, k_b) representing the individual blade (Figure 19). The properties are defined as $m_a = 2,\ k_a = 40,\ m_b = 0.1,\ k_b = 1$.

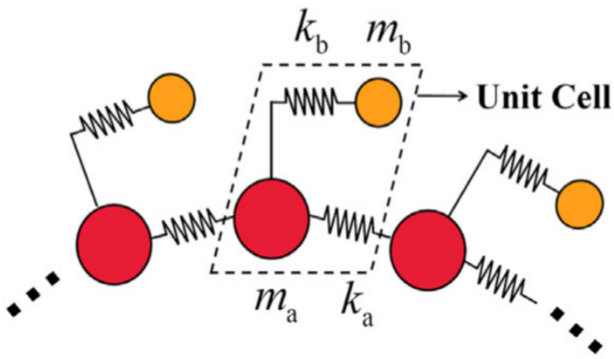

Figure 19 Lumped representation of the blisk [19]

The dynamics of elastic waves propagating through these cyclically periodic unit cells will be analyzed using the transfer matrix method. Defining the state vector $\mathbf{s} = [u, F]^T$, where u is displacement and F is force. Defining the vectors for the adjacent sectors of the one being analyzed:

$$\begin{bmatrix} u_L \\ F_L \end{bmatrix} \ for\ the\ left\ adjacent\ sector \qquad \begin{bmatrix} u_R \\ F_R \end{bmatrix} \ for\ the\ right\ adjacent\ sector \tag{3.1}$$

Since a lumped mass is considered, the displacements to the right and to the left will be equal, $u_L = u_R = u_a$. To analyze the force values, Newton's second law will be utilized. The force equilibrium for the mass m_a can be written as

$$m_a \ddot{u}_a = F_L - F_R + F_{res} \tag{3.2}$$

Where F_{res} is the resonator force coming from the blade of the sector. Similarly, the equilibrium equation for m_b can be written as

$$m_b \ddot{u}_b = -k_b(u_b - u_a) \tag{3.3}$$

Since wave propagation is studied, harmonic solution can be assumed as $u(t) = Ue^{-i\omega t}$. Taking the second derivative with respect to time yields $\ddot{u}(t) = -\omega^2 u(t)$. Substituting into Equation (3.3)

$$-\omega^2 m_b u_b = -k_b(u_b - u_a) \tag{3.4}$$

$$(k_b - \omega^2 m_b)u_b = k_b u_a \tag{3.5}$$

$$u_b = \frac{k_b}{k_b - \omega^2 m_b} u_a \tag{3.6}$$

F_{res} can now be determined

$$F_{res} = k_b(u_b - u_a) = k_b\left(\frac{k_b}{k_b - \omega^2 m_b} u_a - u_a\right) \tag{3.7}$$

$$F_{res} = \left(\frac{\omega^2 m_b k_b}{k_b - \omega^2 m_b}\right) u_a \tag{3.8}$$

Now, substituting F_{res} into Equation (3.2)

$$-\omega^2 m_a u_a = F_L - F_R + \left(\frac{\omega^2 m_b k_b}{k_b - \omega^2 m_b}\right) u_a \tag{3.9}$$

Rearranging to solve for the right-side force F_R

$$F_R = F_L + \omega^2 m_a u_a + \left(\frac{\omega^2 m_b k_b}{k_b - \omega^2 m_b}\right) u_a \tag{3.10}$$

$$F_R = F_L + \omega^2 \left(m_a + \frac{m_b k_b}{k_b - \omega^2 m_b}\right) u_L \tag{3.11}$$

In metamaterial physics, the bracketed term is called frequency-dependent effective mass, m_{eff}.

$$m_{eff} = m_a + \frac{m_b k_b}{k_b - \omega^2 m_b} \tag{3.12}$$

Note that the local blade frequency makes the denominator zero.

Two linear equations relating the right side to the left side now can be written

$$u_R = 1 \cdot u_L + 0 \cdot F_L$$
$$F_R = \omega^2 m_{eff} \cdot u_L + 1 \cdot F_L \tag{3.13}$$

Writing this in matrix form $[u_R \quad F_R]^T = T_{m_a,m_b,k_b}[u_L \quad F_L]^T$, the final transfer matrix becomes

$$\mathbf{T}_{m_a,m_b,k_b} = \begin{bmatrix} 1 & 0 \\ \omega^2 m_{Eff} & 1 \end{bmatrix} \tag{3.14}$$

Similarly, writing the force equilibrium for the inter-sector coupling k_a

$$F_R = k_a(u_L - u_R) \tag{3.15}$$

$$u_R = u_L - \frac{1}{k_a} \cdot F_R \tag{3.16}$$

Assuming the inter-sector stiffness element is massless, the force equilibrium dictates $F_R = F_L$. Therefore, writing in matrix form $[u_R \quad F_R]^T = T_{k_a}[u_L \quad F_L]^T$ yields

$$\mathbf{T}_{k_a} = \begin{bmatrix} 1 & -\frac{1}{k_a} \\ 0 & 1 \end{bmatrix} \tag{3.17}$$

After establishing T_{m_a,m_b,k_b} and T_{k_a}, the global transfer matrix of the unit cell, T_{uc}, is obtained by multiplying them

$$\mathbf{T}_{uc} = \mathbf{T}_{m_a,m_b,k_b}\mathbf{T}_{k_a} = \begin{bmatrix} 1 & 0 \\ \omega^2 m_{Eff} & 1 \end{bmatrix}\begin{bmatrix} 1 & -\frac{1}{k_a} \\ 0 & 1 \end{bmatrix} \tag{3.18}$$

Additionally, by applying Bloch's theorem ([28]), the wave number q of the periodic metamaterial can be extracted from the eigenvalues of the transfer matrix

$$\begin{bmatrix} u_R \\ F_R \end{bmatrix} = \mathbf{T}_{uc}\begin{bmatrix} u_L \\ F_L \end{bmatrix} = \mathrm{e}^{iqd}\begin{bmatrix} u_L \\ F_L \end{bmatrix} \tag{3.19}$$

Where d is the length of one unit cell.

By combining the transfer matrix equation and Bloch's theorem, the governing dispersion relation for the system is derived

$$\left|\mathbf{T}_{uc} - \mathrm{e}^{iqd}\mathbf{I}\right| = \mathbf{0} \tag{3.20}$$

By solving

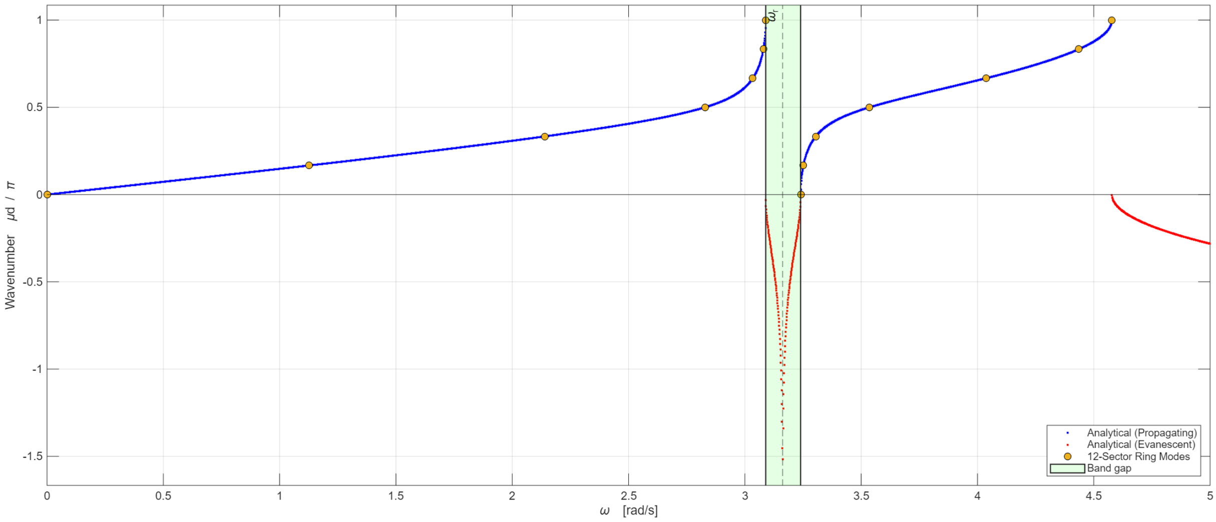

Figure 20 Dispersion graph

As can be seen from Figure 20, the natural frequencies of the lumped blisk model with 12 blades perfectly align with the real part of the dispersion graph, and it represents the phase change in a unit cell. Besides, the imaginary part of the dispersion curve represents the amplitude change ([19]). The 6 modes between [3-3.5 rad/s] are the blade dominated modes. Their corresponding value of natural frequencies are close to each other, although all of them have different nodal diameters. The green strip between [3.09, 3.24] shows the band gap phenomenon that can be seen in metamaterials. That region will be the focus in the next parts. As illustrated in Figure 21, a distinct frequency shift occurs between the 12th and 13th modes, corresponding to the band gap region identified in Figure 20. Within that region elastic waves with a certain frequency are attenuated.

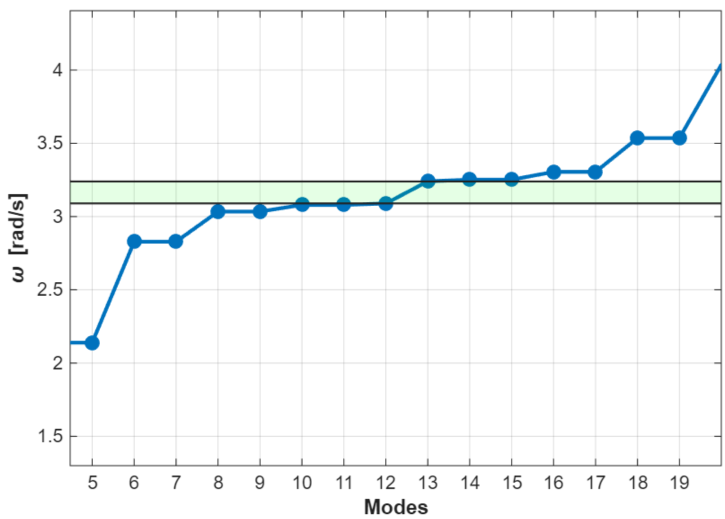

Figure 21 Natural frequency values of different modes for a model with 12 blades

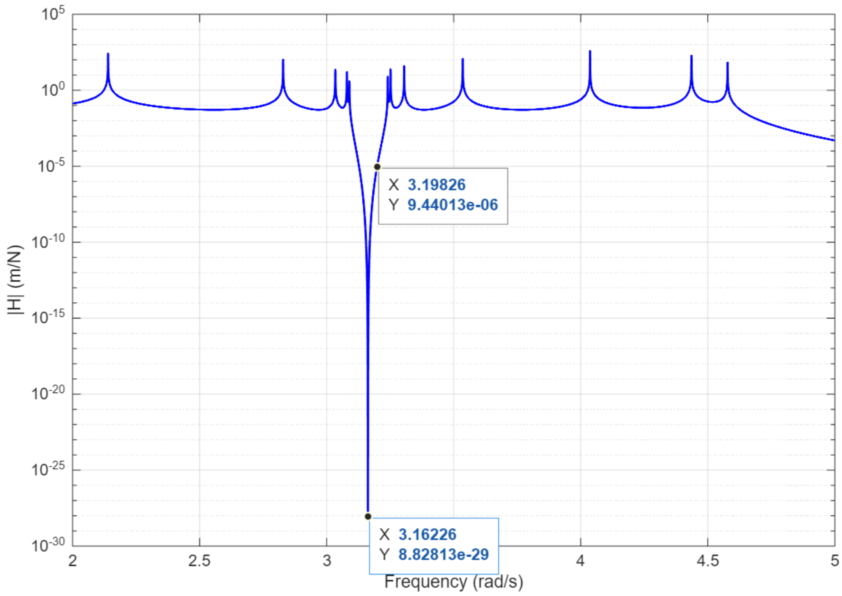

Figure 22 FRF of m_a in the 12th sector

Another graph that the effect of band gap can be seen is FRF plot shown in Figure 22. The mass m_a of the 6th sector is excited and FRF of the mass m_a from the 12th sector is calculated. Choosing sectors on opposite sides of the disk ensures that the elastic wave propagates through multiple stages and allows for clear observation of the attenuation. Within the band gap, a significant decrease in response is shown.

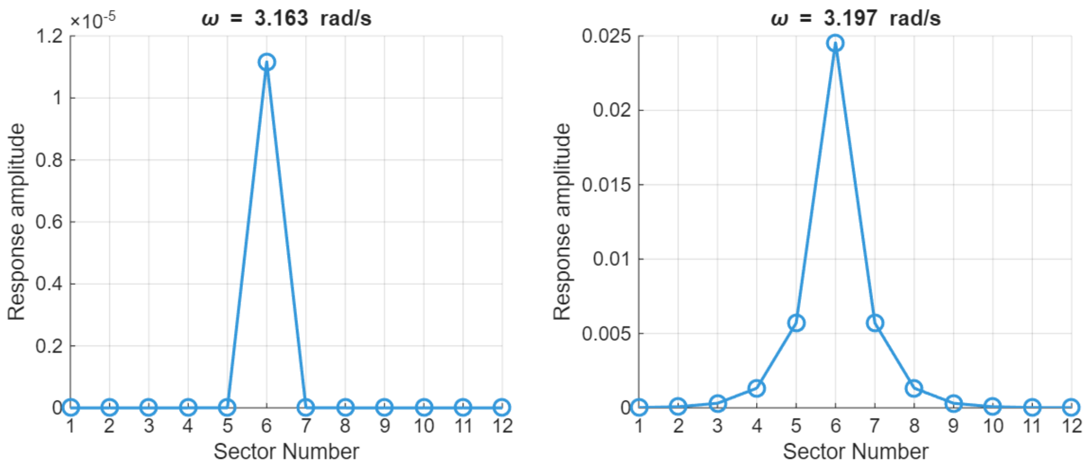

Figure 23 Response amplitudes for the sectors for two different excitation frequencies

Figure 23 shows the absolute response amplitudes across the sectors for two different excitation frequencies, 3.163 and 3.197 rad/s respectively. Like the previous structure, the excitation is again on the m_a of the 6th sector. A clear propagation attenuation is visible as the distance from the source increases. The left plot corresponds to the antiresonance of the blades. At this state, the vibration is highly localized, and the response in sectors other than the excitation sector is extremely low compared to that in the excited sector. Furthermore, the overall vibration magnitude is heavily suppressed, attenuated to the order of 10^{-5} m/N. The second frequency value is still inside the band gap, but different from the antiresonance (Figure 22). In that case, the vibration slightly leaks into the adjacent sectors, and the peak amplitude is significantly higher. The system is still demonstrating strong attenuation away from the excitation point in both scenarios.

To summarize, modeling the bladed disk through the lens of locally resonant metamaterials provides a strong analytical framework for understanding its dynamic behavior. Application of the transfer matrix method to a simplified lumped-mass model shows that the blisk exhibits clear frequency band gaps. Within these specific frequency ranges, the unit-cell effective mass becomes singular, corresponding to the antiresonance of the blades. Consequently, elastic waves are strictly forbidden from propagating circumferentially through the disk, resulting in highly confined vibrational energy within the band gap.

To conclude, the bladed disks are inspected as a metamaterial in this section, comprising cyclical symmetrically arranged unit-cells. Utilizing transfer matrices and Bloch theorem, the dispersion curve of the system is obtained. Elastic wave propagation, and the behavior within the band gap is studied through different graphics.

3.2. Blade-Alone Frequencies

The lumped model in Section 3.1 showed that an antiresonance appears inside the band gap of the cyclic structure. At this frequency, the response of the host mass drops sharply, while the resonator absorbs the energy input. The frequency of this dip is fully determined by the resonator. For the lumped model, it is exactly

$$\omega_{LR} = \sqrt{k_b/m_b} \tag{3.21}$$

which is the natural frequency of the resonator alone with its base held fixed. In the blisk analogy, the resonator is the blade. Therefore, the antiresonance frequency in the FRF of the disk corresponds to the natural frequency of the blade with its root constrained, which is the blade-alone frequency. The same quantity that traditional identification methods try to recover from densely packed resonance peaks ([18]) can now be read directly from a single dip in the response curve.

The equivalence between antiresonance and blade-alone frequency is the basis of the proposed method. Rather than searching for resonance peak, the method searches for antiresonance dips. Two advantages follow. First, antiresonances are local features of the FRF and are far less sensitive to damping and to small modelling errors than resonances ([29], [30]). Second, a dip is much easier to locate than a closely spaced cluster of blade-dominated resonances.

The equivalence is, however, strictly valid only for the lumped model. For a real blade a small error is introduced. The origin of the error has a clean physical interpretation from the point of view of wave propagation, illustrated in Figure 24.

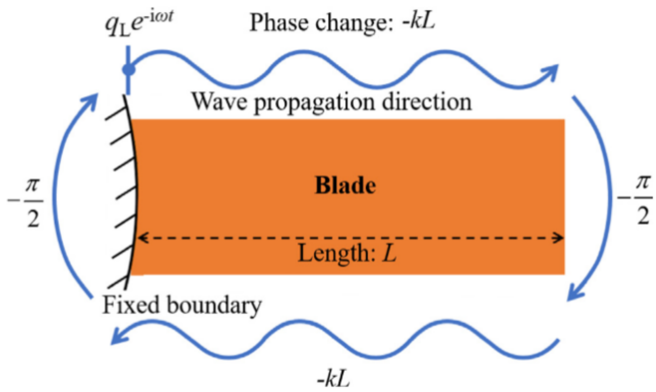

Figure 24 Wave propagation along cantilever beam[19]

Consider the blade as a uniform cantilever beam of length L. A flexural wave inside the blade can be written as

$$u(x,t) = Ae^{i(kx-\omega t)} \tag{3.22}$$

Where k is the wavenumber. The wave travels from the root to the tip and back. Along the blade it accumulates a phase change of $-kL$ in each direction, for a total of $-2kL$ over one round trip ([31]). At each end the wave is reflected. For an Euler-Bernoulli beam, both the free tip and the clamped root contribute a reflection phase of $-\pi/2$, as indicated on the left and right boundaries of Figure 24 ([31]). At the natural frequencies of the isolated cantilever blade, the sum of all contributions over one round trip is a multiple of -2π, which is the phase closure condition.

Suppose now that the clamped end is released and the wave is allowed to continue into the disk. Only the reflection at the tip survives, so the phase accumulated along the blade alone becomes $-2n\pi + \pi/2$. The shear force transmitted into the disk is proportional to the third spatial derivative of the deflection and is therefore shifted by a further $\pi/2$ with respect to the deflection wave. Summing up the two contributions, the total phase difference between the shear force coming from the blade and the deflection of the disk at the root is $-2n\pi + \pi$. The two quantities are in anti-phase. The force coming from the blade cancels the external force applied to the disk, and the response of the disk drops. The mechanism just described is the physical origin of the antiresonance ([19], [32]).

The derivation above is approximate. A $-\pi/2$ reflection phase assumes that only the propagating part of the flexural wave is present at the boundary. In practice, an evanescent component also appears at each end ([31]). It decays exponentially over a distance comparable to the wavelength and modifies the effective reflection phase. At high frequencies, where the wavelength is short, the correction is negligible. At the first bending mode, which is in the frequency range of interest in this work, the wavelength is comparable to the blade length, and the correction is no longer small. As a consequence, the antiresonance frequency observed in the disk FRF is slightly shifted with respect to the true blade-alone frequency.

The shift cannot be removed by refining the analytical deviation, since the evanescent field depends on the geometry of the blade-disk junction. A different route is therefore adopted in the present work: the measurement is corrected, not the theory. The starting observation is that the antiresonance frequency seen in the FRF depends on where the response is measured. Moving the sensor along the structure shifts the position of the dip, and at least one location can always be found where the observed antiresonance frequency coincides with the true blade-alone frequency. Finding that location is the task of the Measurement Point Correction (MPC), described in the next section.

3.3. Measurement Point Correction (MPC) Strategy

Section 3.2 ended with the observation that the antiresonance frequency seen in the FRF depends on where the response is measured. The Measurement Point Correction (MPC) strategy turns this dependence into an advantage: rather than treating the spatial variation of the dip as a source of uncertainty, it is exploited to recover the true blade-alone frequency from a single, well-chosen measurement point.

The strategy is based on two ingredients. The first is a reference value of the blade-alone frequency obtained from a separate, simple calculation. The second is a map of antiresonance frequencies across the sector, obtained from a harmonic response analysis of the full blisk. Comparing the two identifies the optimal sensor location. The reference value is computed in a single sector. The blade is isolated from the disk by constraining all the degrees of freedom at the blade root. A standard modal analysis then yields the natural frequencies of the cantilever blade. The frequency of the first bending mode, denoted f_{ba}, is the target value that the antiresonance dip must reproduce. This calculation is inexpensive, fully deterministic, and depends only on the nominal blade geometry and material.

The second ingredient comes from a harmonic response analysis of the full nominal blisk. The boundary conditions reproduce those of the actual experiment or simulation in which the identification will be performed: only the center of the disk is constrained, and the excitation point is fixed near the root of one blade. The detuning masses described in Section 3.4 are placed on all blades except the one under test, in order to isolate a single antiresonance peak in the frequency band of interest.

The FRF is then computed at every node of one sector over a frequency range that contains the band gap. For each node, the antiresonance frequency closest to f_{ba} is extracted by locating the deepest minimum of the response. The result is a scalar field of antiresonance frequencies defined over the sector, which can be visualized as a color map (Figure 36 in Section 4.4 shows this map for the dummy blisk used in this work).

The optimal measurement point is the node whose antiresonance frequency is closest to f_{ba}. By construction, when the sensor is placed at that node, the dip observed in the FRF directly returns the blade-alone frequency, and the systematic shift caused by the evanescent field at the blade–disk junction (Section 3.2) is removed.

In practice, the antiresonance field is smooth, and the locus of points satisfying the matching condition is not a single isolated node but a continuous contour on the sector. Any point on this contour is, in principle, an acceptable measurement location. This flexibility is useful in experimental implementation, since it allows the sensor to be placed at a position that is also convenient from a practical point of view, such as a flat area of the blade surface where an accelerometer can be reliably bonded.

The MPC is performed once on the tuned nominal model, and the resulting measurement point is then used for every blade in the mistuned identification process. The implicit assumption is that the optimal location does not change significantly when small mistuning is introduced. This assumption is reasonable for two reasons. First, the magnitude of mistuning associated with manufacturing tolerances is small, typically of the order of one to a few percent, and is known to leave the blade-disk coupling essentially unchanged ([4]). Second, since the antiresonance contour identified above is broad, a small redistribution of the field around the selected node keeps the measurement point inside the acceptable region.

The MPC therefore decouples two distinct questions: a geometric one, namely, where to measure, and a dynamic one, namely what each blade contributes. Once the optimal point has been selected on the tuned model, the blade-by-blade detuning procedure described in the next section can be applied without re-running the correction for every mistuning pattern.

3.4. Blade-by-Blade Numerical Detuning Strategy

With the measurement point fixed by the MPC strategy, the identification proceeds blade by blade. The goal of each individual test is to isolate the antiresonance associated with a single blade, so that its frequency can be unambiguously extracted from FRF.

The procedure follows the same logic as the classical detuning strategy used in resonance-based identification ([17], [33]). A small point mass is added at the tip of every blade except the one under test. The mass shifts the blade-alone frequency of the loaded blades away from the nominal value, while the unloaded blade keeps its original frequency. In the FRF of the disk, only one antiresonance dip remains in the frequency band of interest, and it corresponds to the blade under test.

The procedure is repeated for each of the *N* blades. At every iteration the detuning masses are relocated so that the test blade is the only one without an added mass. The excitation point and the measurement point are also moved accordingly, in order to remain in the sector of the blade under test. The result is a set of *N* antiresonance frequencies one for each blade.

$$f_i^{a(n)}, \qquad n = 1,2, \dots N$$

The detuning strategy used here serves a different purpose than in resonance-based methods. In the resonance approach, the detuning masses are intended to suppress inter-blade coupling and produce a clean resonance peak for the isolated blade. In the present antiresonance framework, the suppression of coupling is already partially achieved by the choice of the measurement point through the MPC. The detuning masses are needed only to ensure that the antiresonances of the other blades do not overlap with the one being measured. Residual inter-blade coupling, which is the main source of error in resonance-based detuning tests ([18], [33]), affects the present method only marginally.

The set f_i^a obtained from blade-by-blade test is the raw output of the identification procedure. The next section explains how it is converted into the mistuning patterns of blade frequency and Young's modulus.

3.5. Extraction of Mistuning Patterns (Frequency and Young's Modulus)

The blade-by-blade detuning procedure described in Section 3.4 produces a set of N antiresonance frequencies, $f_i^{a(n)}$, one for each blade of the blisk. Thanks to the antiresonance-blade-alone equivalence established in Section 3.2 and to the correction introduced by the MPC, each value f_i^a is a direct estimate of the blade-alone frequency of the corresponding blade. The final step of the method consists in converting these frequencies into a mistuning pattern that quantifies the deviation of each blade from a nominal reference.

The natural quantity to describe mistuning is the relative deviation of the blade-alone frequency from a reference value. For the i-th blade, the frequency mistuning is defined as

$$\delta_i^f = \frac{f_i^a - f_{ref}}{f_{ref}} \tag{3.23}$$

The reference frequency f_{ref} is the blade-alone frequency of a blade with nominal material properties, namely the value computed from a modal analysis of a single sector with $E = E_0$ and the root constrained. In the present work, $E_0 = 200{,}000\ MPa$ is used as the nominal Young's modulus, and f_{ref} is therefore the first bending frequency of a cantilever blade with this elastic modulus. The choice has the advantage of providing an absolute, model-independent reference: the identified mistuning of every blade is measured against the same fixed quantity.

The vector $\boldsymbol{\delta}^f = \{\delta_1^f, \delta_2^f, \dots, \delta_N^f\}$ is the frequency mistuning pattern of the blisk. It is the primary output of the identification procedure and contains all the information needed to update the dynamic model of the structure.

For most applications, and in particular for the finite element model used in Chapter 4, mistuning is parametrized in terms of Young's modulus rather than the natural frequency. The two quantities are related through the dynamic equations of the blade.

For a uniform cantilevered beam under flexural vibration, the natural frequency of the n-th bending mode is given by [34]

$$f_n = \frac{(\beta_n L)^2}{2\pi L^2}\sqrt{\frac{EI}{\rho A}} \tag{3.24}$$

Where I is the second moment of area, A the cross-sectional area, ρ the density and $\beta_n L$ a non-dimensional constant depending on the mode shape. All geometric and mass terms are unaffected by the type of mistuning considered here, so the proportionality

$$f \propto \sqrt{E} \tag{3.25}$$

Holds for each individual blade. Squaring both sides and taking the relative deviation yields the relationship between the two mistuning patterns:

$$\delta_i^E = \frac{E_i - E_0}{E_0} = \left(1 + \delta_i^f\right)^2 - 1 \approx 2\delta_i^f \tag{3.26}$$

The last approximation is valid for small mistuning, $\left|\delta_i^f\right| \ll 1$, which is the regime of practical interest. The identified Young's modulus of the i-th blade is then

$$E_i = E_0\left(1 + \delta_i^f\right)^2 \tag{3.27}$$

The vector $\boldsymbol{\delta}^E = \{\delta_1^E, \delta_2^E, \dots, \delta_N^E\}$ is the Young's modulus mistuning pattern of the blisk and can be inserted directly into the FE model as a sector-by-sector modification of the elastic properties of the blades.

It is worth noting that the conversion above implicitly assumes that mistuning is purely stiffness-based, that is, the geometry and the mass of each blade are equal to their nominal values. If a real blade also exhibits a small mass deviation, the $\sqrt{E}$ relation absorbs the combined effect into an equivalent stiffness perturbation, which is still a useful, although not exact, representation of the true mistuning.

Once the mistuning pattern is known, the FE model of the nominal tuned blisk is updated by assigning the identified Young's modulus to each blade. The updated model can then be used to predict the forced response of the actual mistuned blisk under any prescribed excitation, in particular under engine-order excitation representative of operational aerodynamic loads.

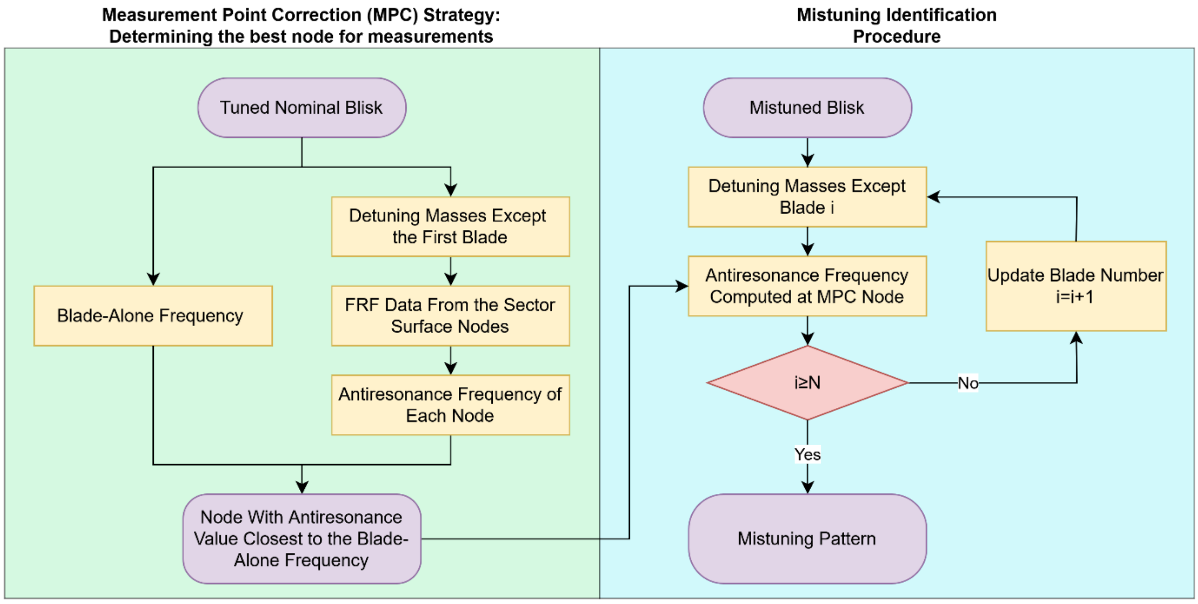

Figure 25 Flowchart of methodology

Figure 25 shows the steps followed to apply the methodology which is carried out in the next chapter. Two main routes branch from the tuned and the mistuned blisk. The first route uses the nominal blisk to determine the best measurement point through the MPC strategy described in Section 3.3. The blade-alone frequency is computed on a single sector, while the FRF data of the sector surface nodes are extracted from the detuned model and the antiresonance frequency of each node is obtained. The node whose antiresonance value is closest to the blade-alone frequency is selected as the measurement point. This route is run only once: because it relies on the nominal model, the measurement point does not need to be recomputed for each blade or for a different mistuning pattern.

The second route starts from mistuned blisk. The detuning strategy isolates the blade under test, and its antiresonance frequency is computed at the measurement point fixed by the first route. The procedure is repeated blade by blade until all blades are covered. Each identified antiresonance frequency is a direct estimate of the blade-alone frequency of the corresponding blade, and these values are converted into the frequency and Young's modulus mistuning patterns defined in Section 3.5, which form the final output of the method. A numerical validation of these steps is presented in the next chapter, where the identified pattern is compared with a known mistuning imposed on the model.

4. Numerical Validation and Discussion

The present chapter validates the identification methodology developed in Chapter 3 on a finite element model of a simplified bladed disk. The objective is to verify, in a controlled numerical environment, the three claims on which the method rests: that the antiresonance dip observed in the disk frequency response function reproduces the blade-alone frequency once a suitable measurement point is selected (Section 3.2), that the Measurement Point Correction strategy successfully removes the systematic shift caused by the evanescent field at the blade-disk junction (Section 3.3), and that the blade-by-blade detuning procedure yields, for each sector, an antiresonance frequency that can be converted into a quantitative estimate of the Young's modulus mistuning of the blade (Section 3.4 and Section 3.5). To this end, a dummy blisk with twelve sectors and a prescribed mistuning pattern is built in ANSYS Mechanical 2025b. Because the Young's modulus of every blade is imposed by the user, the ground truth of mistuning pattern is known exactly, and the accuracy of the identification can be assessed without ambiguity. The chapter is organized along with the same logical sequence followed in Chapter 3. Section 4.1 describes the geometry, the material properties, and the mistuning pattern assigned to the model. Section 4.2 reports the reference blade-alone frequencies obtained from a constrained-root modal analysis on a single sector. Section 4.3 performs the harmonic response of the full mistuned blisk and displays the effect of the detuning masses on the FRF. Section 4.4 implements the Measurement Point Correction on the tuned configuration of the model and identifies the optimal measurement location. Section 4.5 applies the blade-by-blade detuning procedure to the mistuned blisk and compares, for every blade, the identified antiresonance frequency with the reference blade-alone frequency. Section 4.6 compares the imposed and identified mistuning values, and finally Section 4.7 explains the procedure for resonance-based identification method before comparing the results coming from the antiresonance-based and resonance-based methods.

4.1. Model Description and Setup

The methodology developed in Chapter 3 is validated on a dummy blisk consisting of twelve geometrically identical sectors. The host disk has an outer radius of 120 mm and a central clamping hole of 20 mm, and each blade is 200 mm long and 48 mm wide. A uniform thickness of 10 mm is assigned to the entire structure, so that both the disk and the blades share the same out-of-plane dimension. The two-dimensional geometry of the model is shown in Figure 26.

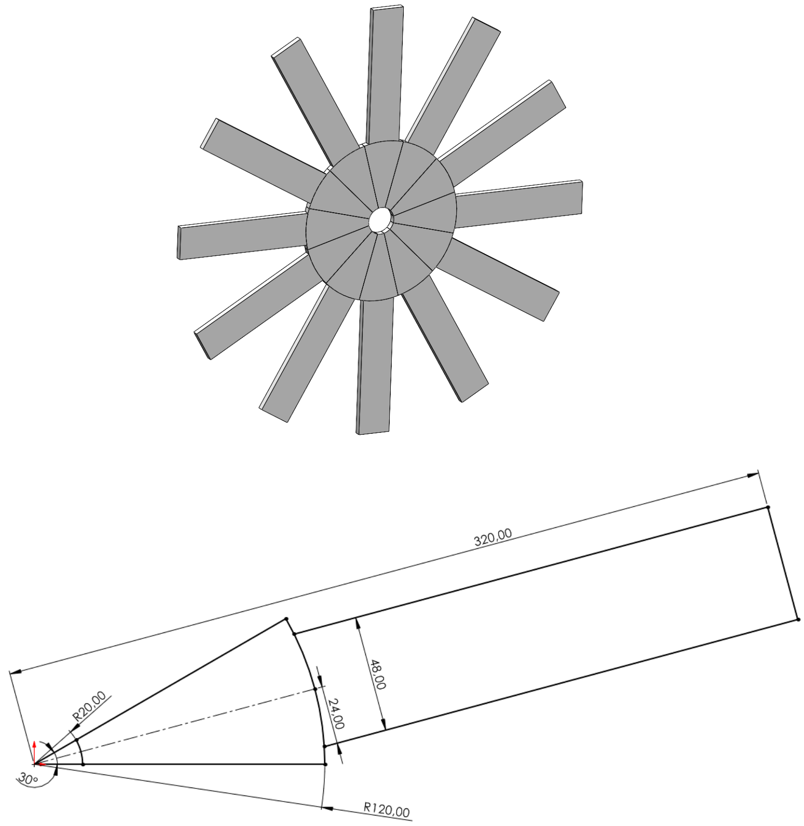

Figure 26 The dummy blisk used in analyses

A model with simplified geometry is deliberately chosen. A realistic model of a rotor would introduce features that affect dynamic behavior in a way that is difficult to isolate. Some of these features include blade twist, airfoil shape, and fillet geometry at the blade root. The dummy blisk used in this chapter removes these confounding factors. It only consists of structural ingredients that are essential to the proposed identification method. The dummy blisk shows a clear cyclical symmetry, includes a host disk that couples adjacent sectors, and a set of blades whose first bending mode falls within an easily resolvable frequency range. The first bending mode family can be seen in Figure 27, as the bottom blue line. The user can then manually impose the mistuning pattern, establishing an exact reference to validate the identification method.

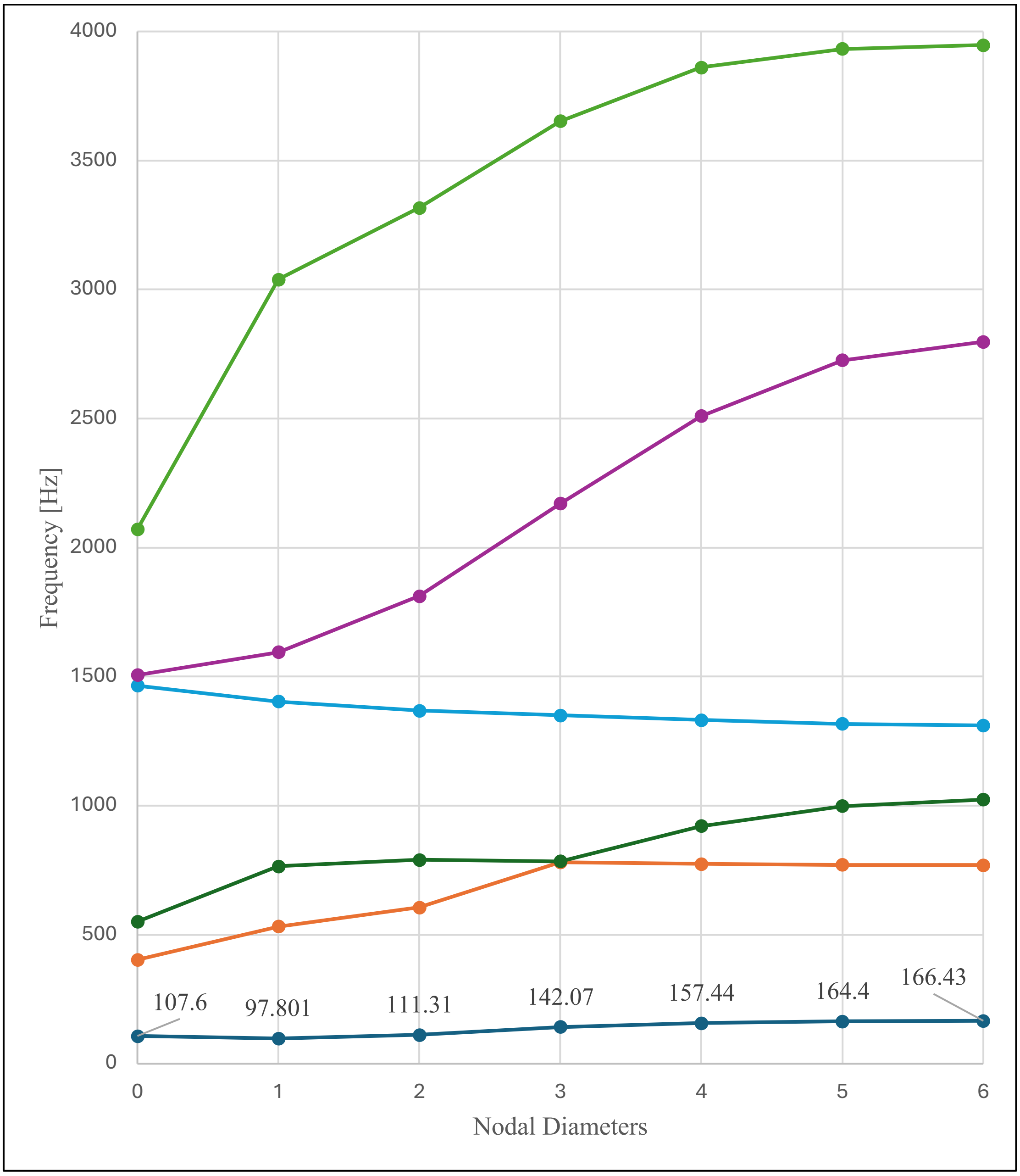

Figure 27 Nodal diameters of the tuned model

The finite element analysis is performed in ANSYS Mechanical 2025 R2. Structural steel is selected as the nominal material, with Young's modulus $E_0 = 200{,}000\ MPa$, density $\rho = 7{,}850\ kg/m^3$, and Poisson's ratio $\nu = 0.3$. Mistuning is introduced exclusively through the Young's modulus of the blades, in accordance with the small-mistuning assumption discussed in Section 1.6. The Young's modulus of the shared disk is uniform and equal to E_0, so the disk can be considered as tuned. The values for the blades are changed according to Table 2. The shift from the nominal value as a percentage is at most 3% on Blade 8.

Table 2 Young's modulus values for the blades

Blades	Young's modulus [GPa]	δ_i^E [%]
Blade 1	200	0
Blade 2	203	1.5
Blade 3	195.8	-2.1
Blade 4	201.6	0.8
Blade 5	197.6	-1.2
Blade 6	205	2.5
Blade 7	199	-0.5
Blade 8	206	3
Blade 9	194.4	-2.8
Blade 10	202.2	1.1
Blade 11	196.4	-1.8
Blade 12	200.8	0.4

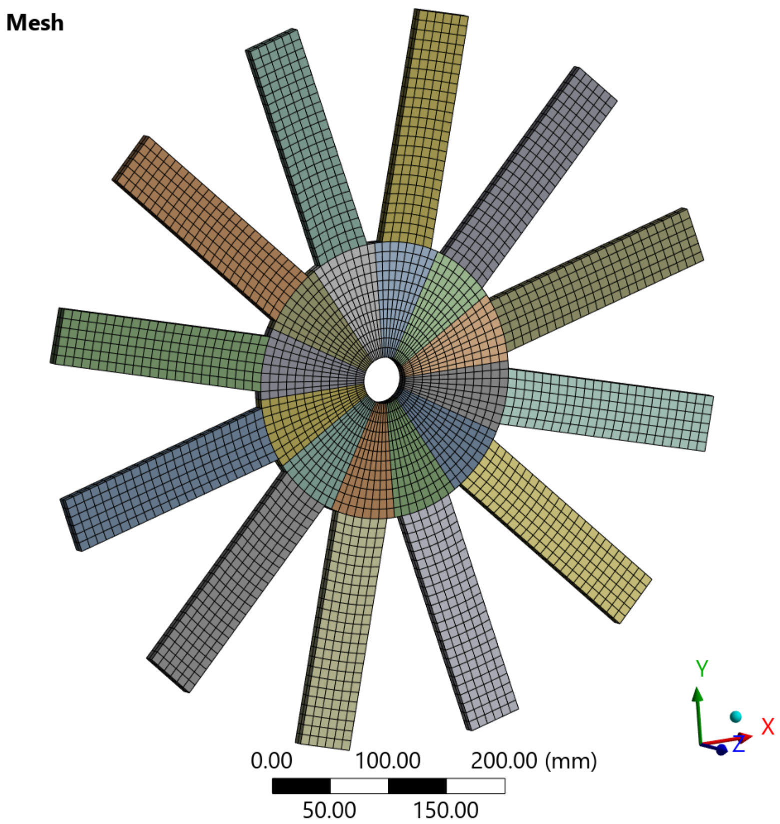

Figure 28 The mesh of the structure

For every analysis in this chapter, the structure is discretized using a structured hexahedral mesh, shown in Figure 28. In total, 34,752 nodes and 5,760 elements are present in the model. An edge sizing method is deliberately applied to ensure there are two elements along the width, thereby increasing accuracy. The relevant boundary conditions will be explained in the corresponding chapters.

4.2. Reference Blade-Alone Frequencies

The reference blade-alone frequency for each blade is obtained from a modal analysis of entire model with the mistuning values presented in Table 2. The cantilever beam analogy defines the blade-alone frequency, as introduced in Section 3.2. This condition is imposed by adding fixed constraints to all the disk nodes, see Figure 29.

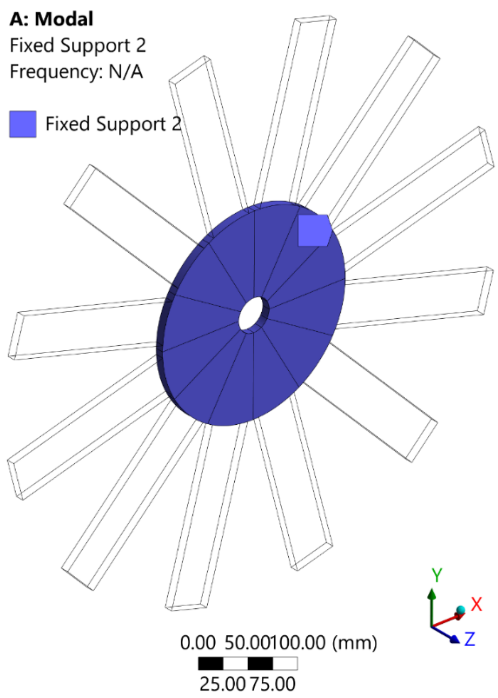

Figure 29 Fixed support defined for the modal analysis of blade-alone frequencies

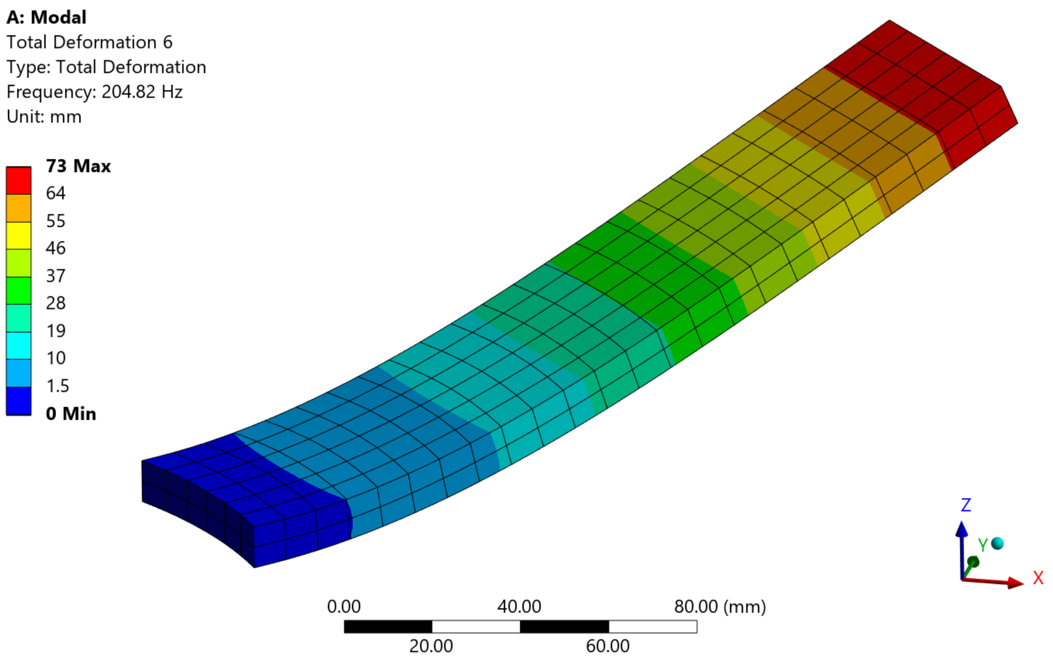

Figure 30 The mesh and the first bending mode of the blade 1

The first bending mode frequencies obtained from the analysis are reported in Table 3. These twelve values constitute the ground truth of the validation: every identified antiresonance frequency in Section 4.4 will be compared against the corresponding entry of this table. The first bending frequency of Blade 1 represents the nominal blade-alone frequency, and it will be used as a reference frequency for the presented method.

Table 3 The frequencies of first bending modes of the blades

Blades	Frequency [Hz]	Blades	Frequency [Hz]
Blade 1	**204.82**	Blade 7	204.31
Blade 2	206.35	Blade 8	207.87
Blade 3	202.66	Blade 9	201.94
Blade 4	205.64	Blade 10	205.95
Blade 5	203.59	Blade 11	202.97
Blade 6	207.37	Blade 12	205.23

4.3. Harmonic Response and Detuning Results

The harmonic response analysis is performed on the full mistuned blisk with the mesh of Figure 28. The Young's modulus pattern of Table 2 is used, and a uniform structural damping coefficient of 0.002 is assigned to the model. This damping value is representative of the structural damping value typically reported for metallic blisks. The only boundary condition defined for this case is the fixed constraint applied to the nodes of the inner hole of the host disk. A unit harmonic nodal force of 1 N is applied along the axial direction at a node located near the root of blade 1, marked by a red ribbon in Figure 31, and the FRF is computed at the same node. The full solution method is selected instead of mode superposition to achieve more accurate results, although it is computationally more expensive.

The resulting frequency response function is shown in Figure 33, together with the deflection shapes along axial direction evaluated at the three different local minima. The red point on the models is used both for excitation and for calculating the FRF. The three dips to inspect are selected at 103.5 Hz, 137 Hz, and 169 Hz. These frequencies correspond to distinct antiresonance candidates of the full mistuned system. The system's vibratory response at the first two frequencies is distributed across different sectors. At 169 Hz, by contrast, the response localizes almost entirely on blade 1 while remaining sectors stay nearly at rest, indicating that blade 1 is effectively decoupled from the assembly. This dip is therefore identified as the antiresonance associated with the blade-alone behavior of blade 1, whereas the dips at 109 Hz and 138 Hz arise from the multi-blade dynamics and are not relevant to the identification.

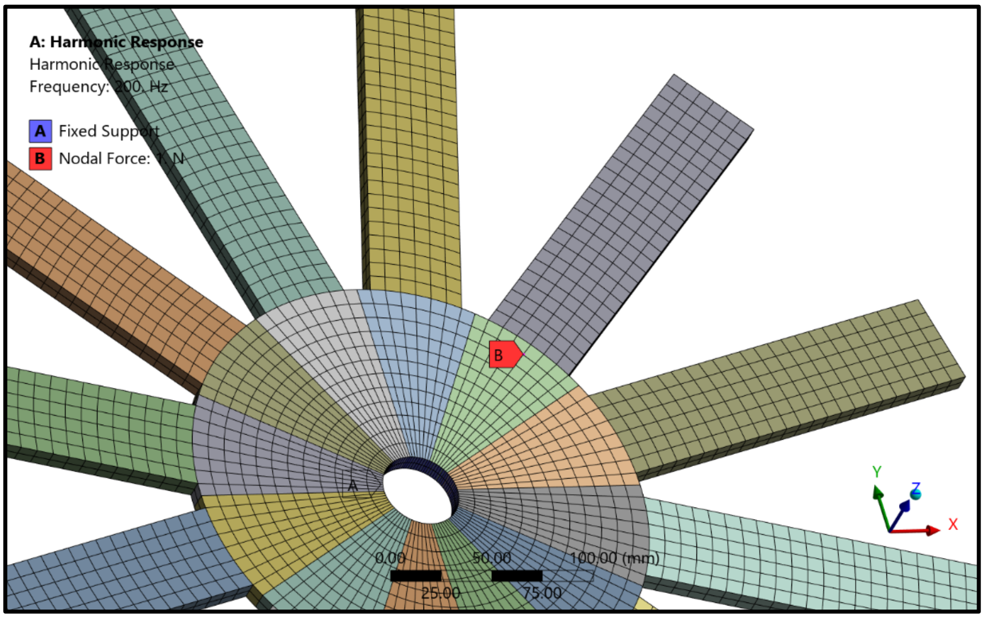

Figure 31 Boundary condition and excitation point

Figure 33 show the FRF but with the numbers on it which represent the resonances and antiresonances of the mistuned model. The deformation shapes for the resonances are presented in Table 4 and for the antiresonances are presented in Table 5. Although the forcing is not defined as engine order excitation, the deformations 1, 3, 5, 7, and 9 are quite similar to modal shapes with nodal diameters.

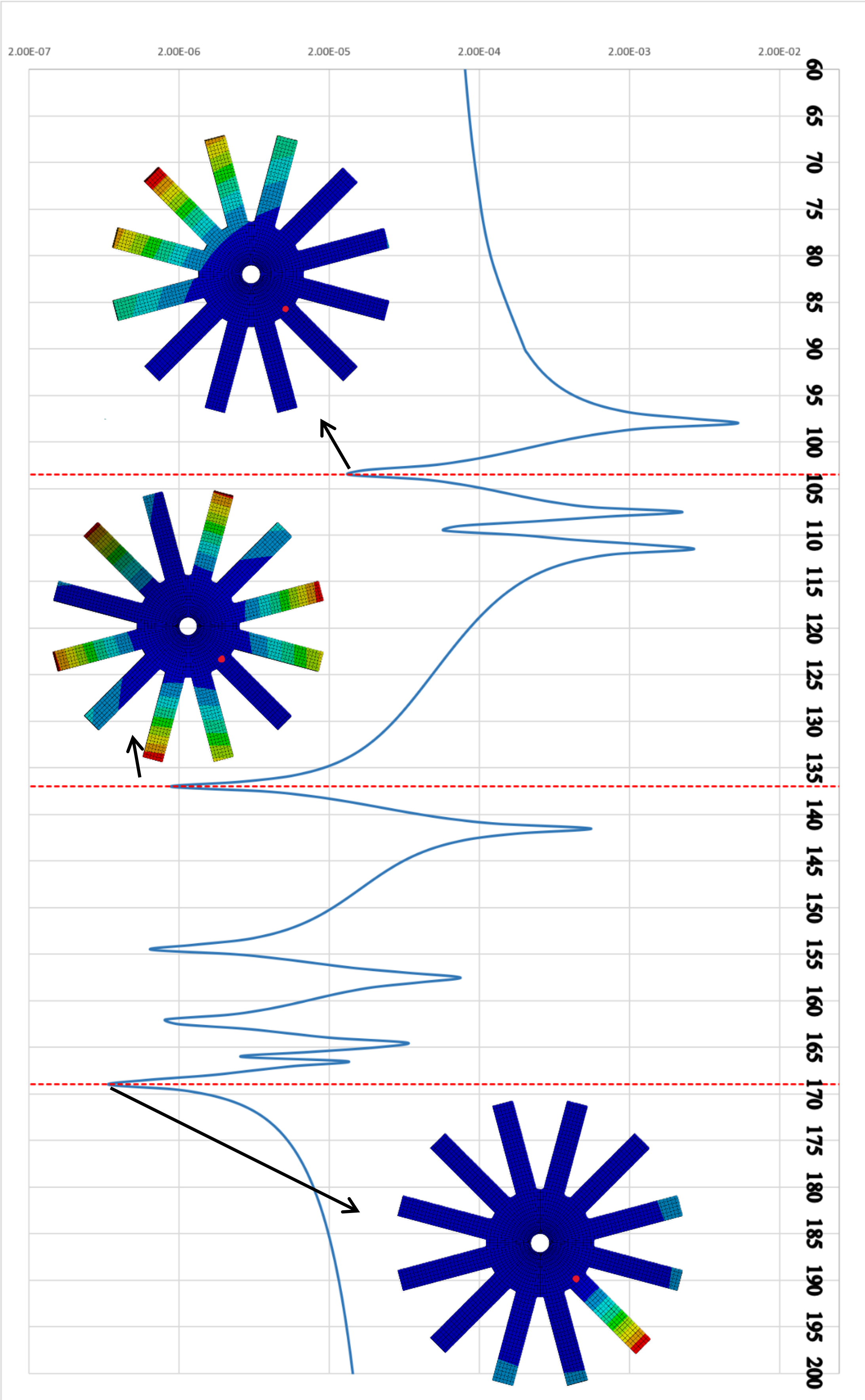

Figure 32 FRF of the mistuned blisk with 3 different antiresonance shapes

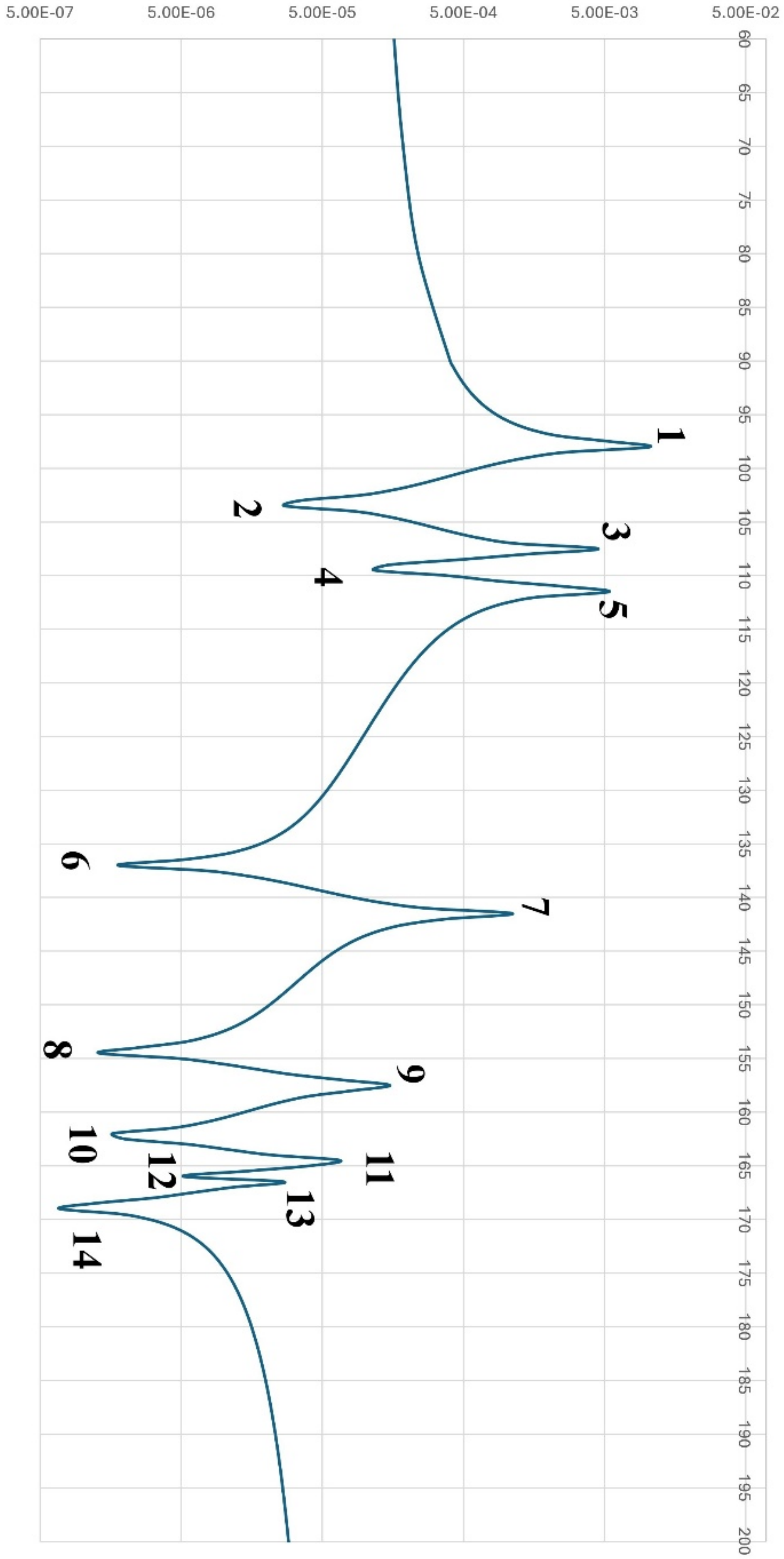

Figure 33 FRF of the mistuned bladed disk

Table 4 Deformation shapes of resonance frequencies (1,3,5,7,9,11,13)

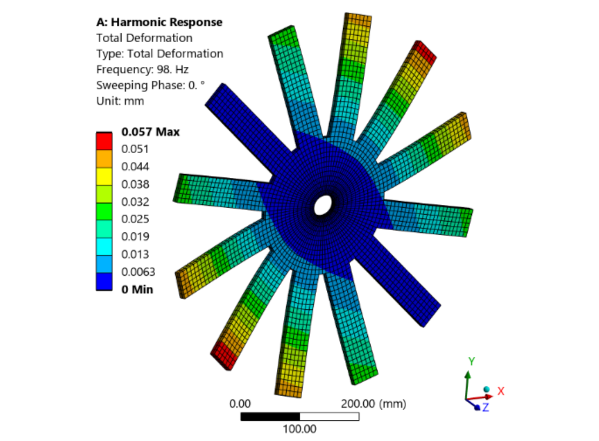

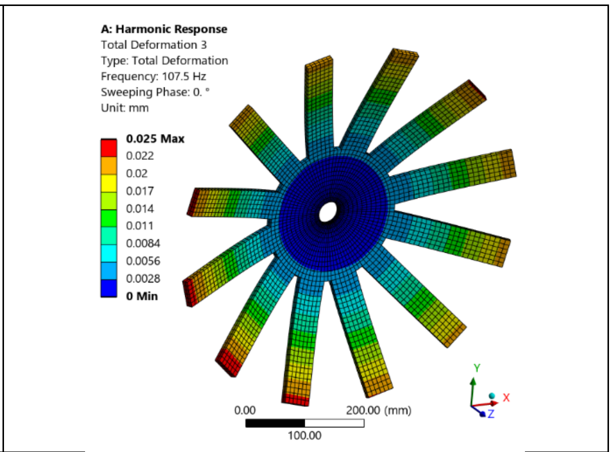

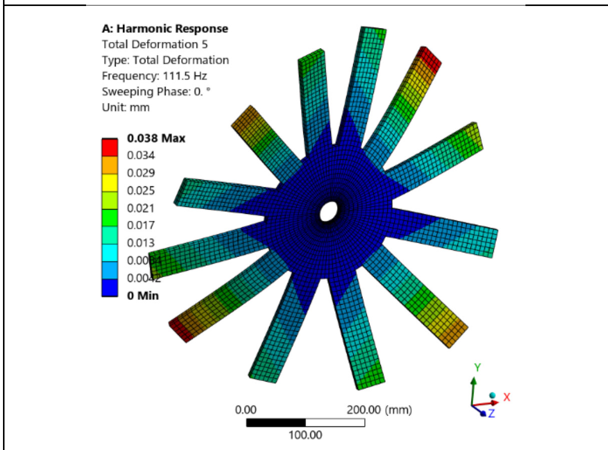

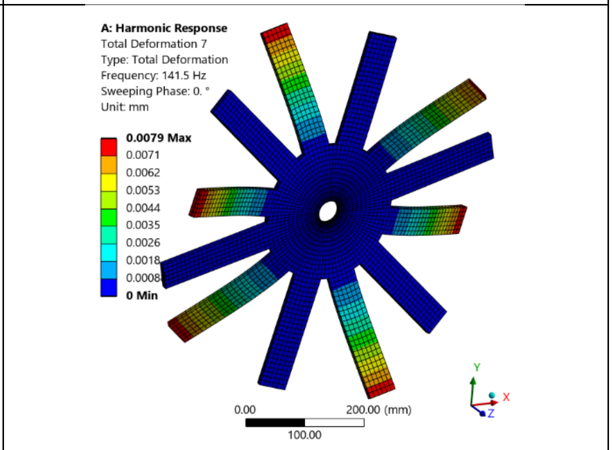

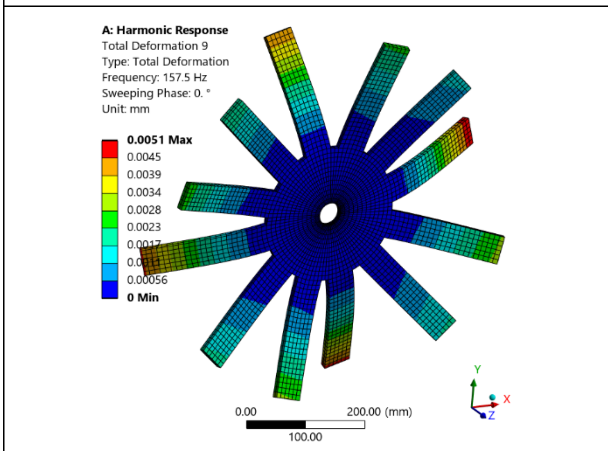

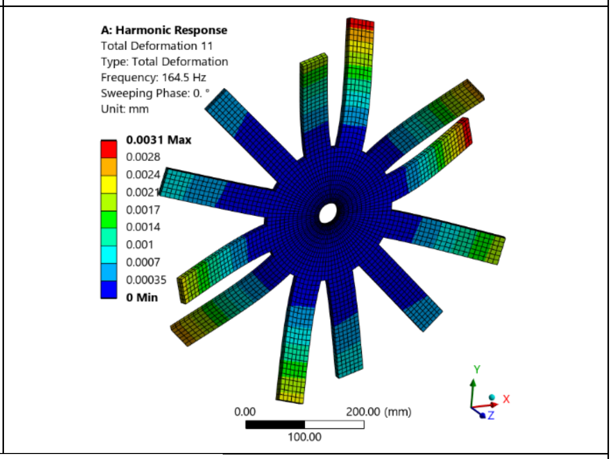

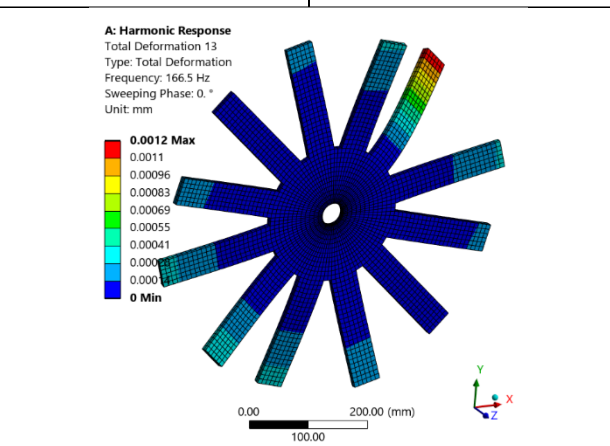

Table 5 Deformation shapes of antiresonance frequencies (2,4,6,8,10,12,14)

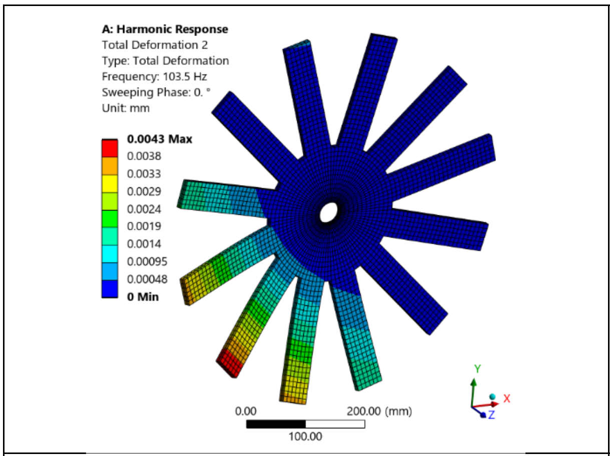

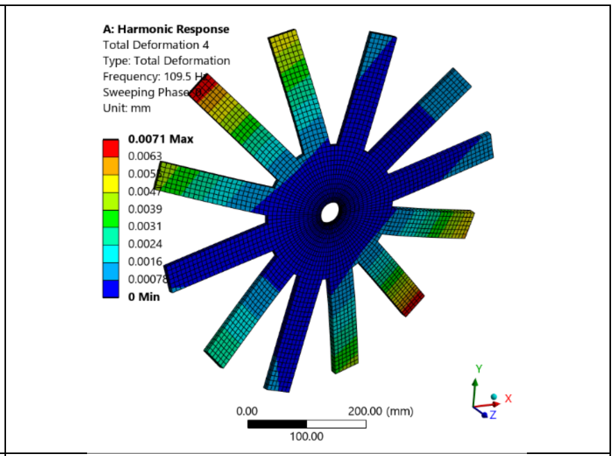

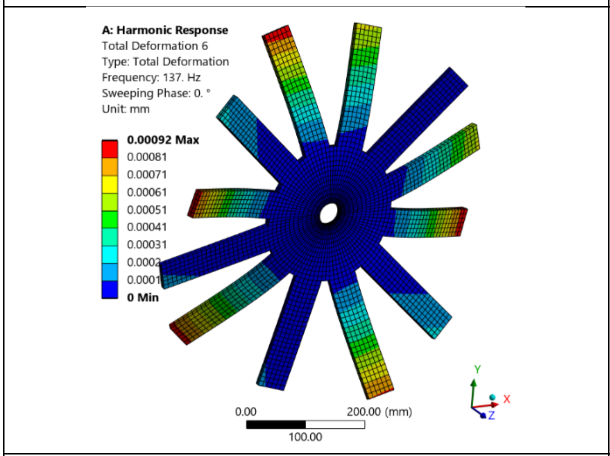

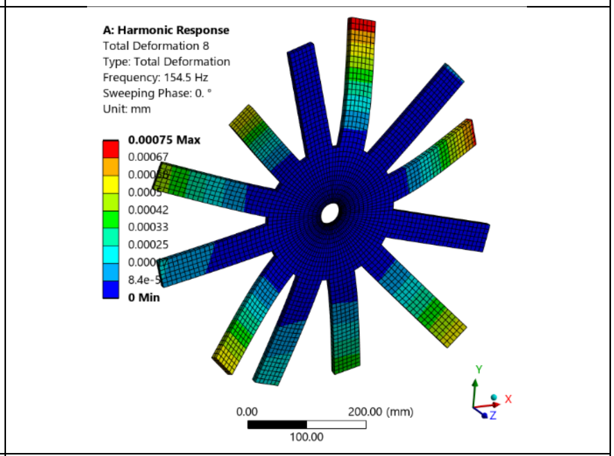

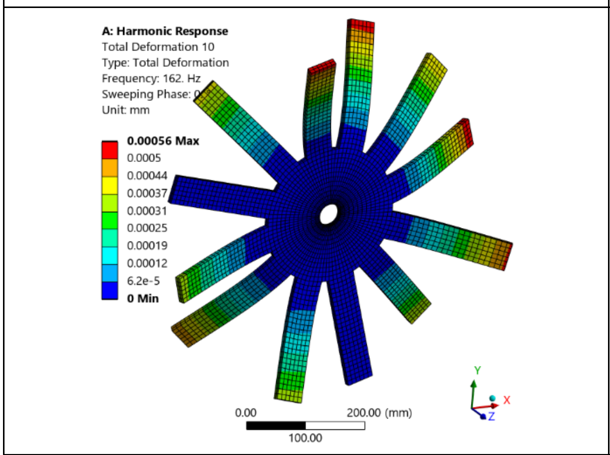

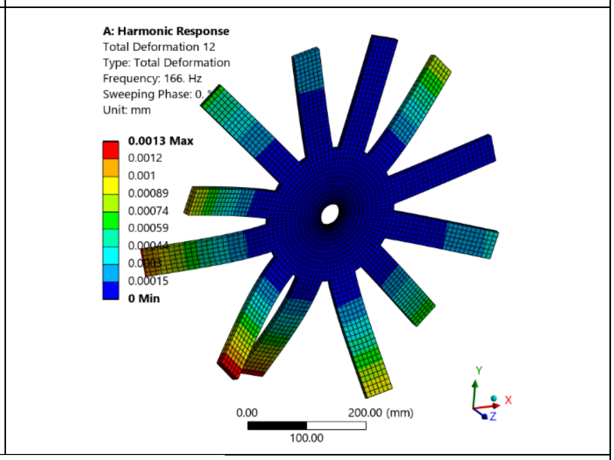

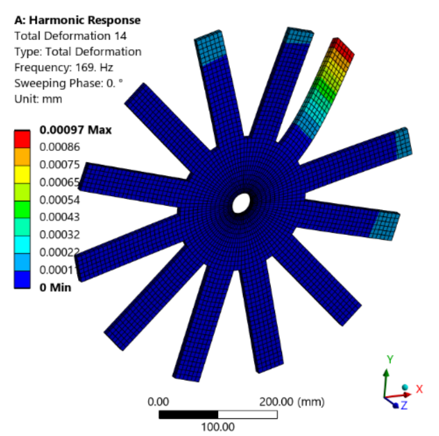

The detuning point masses with a mass of 0.5 kg are added to the tip of each blade except for the blade 1 to isolate it (Figure 34). The harmonic response analysis is then repeated after applying the detuning strategy described in Section 3.4. Through ANSYS Mechanical's geometry options, a point mass of 0.5 kg is added at the tip of each blade except blade 1, as shown in Figure 34. The added masses lower the blade-alone frequencies of the loaded blades and move them outside the frequency band where the antiresonance of blade 1 is expected. As a result, the antiresonances of the eleven loaded blades no longer compete with the dip of interest.

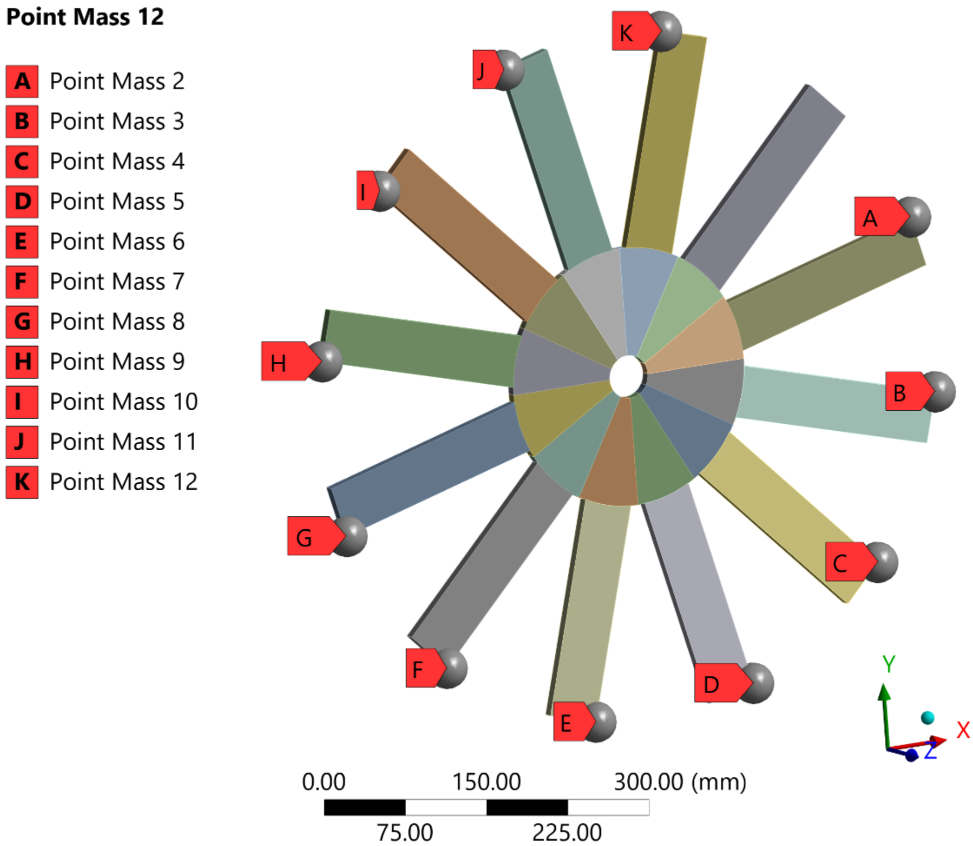

Figure 34 Added detuning masses

The FRF of the detuned configuration is shown in Figure 35, alongside the deflection shape along axial direction evaluated at the antiresonance frequency. The FRF is again computed by using the same node as excitation. A single sharp dip is now visible in the relevant region, located at 168 Hz. The deflection shape shows that the response is localized on the unloaded blade while all other sectors remain almost at rest. A shift in frequency from 169 Hz to 168 Hz is noticeable and consistent with the total mass increase of 5.5 kg due to added masses. The dips at 103.5 Hz and 137 Hz, visible in the response without detuning masses, are no longer present in the relevant frequency band. Consequently, the detuning masses effectively isolate the antiresonance of the blade under test.

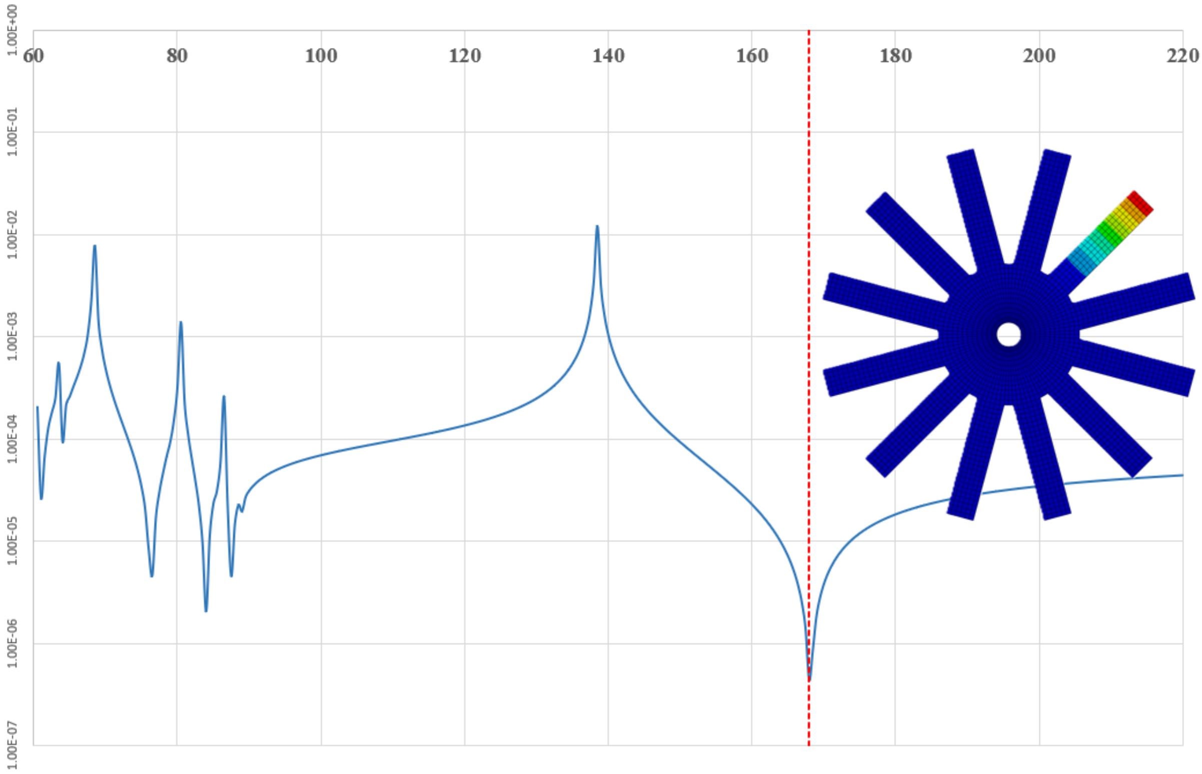

Figure 35 FRF of the mistuned blisk with detuning masses

As noted in the literature, a residual inter-blade coupling through the shared disk persists even after the detuning procedure ([18], [35]). The quantification of this residual coupling is beyond scope of the present work. However, the next sections will show that its effect on the identified antiresonance frequencies is small enough to keep the relative error of the identification below one percent.

4.4. Measurement Point Correction Results

A tuned blisk with homogeneous material properties is used to implement the measurement point correction (MPC) strategy. Detuning masses are added again, except for the first blade, and the harmonic response analysis mentioned in Section 4.3 is repeated. The nodes on the sector's top surface without detuning mass are selected and grouped into a named selection in ANSYS. Using the automation code provided in Appendix A, the frequency response values for the range of 50-250 Hz are extracted as text files. These files are then analyzed by using the PYTHON code in Appendix B to determine the antiresonance value of the nodes. After these steps, the coordinates and antiresonance frequencies of the selected nodes are stored in a single file for importing into MATLAB. Figure 36 is created using the MATLAB code supplied in Appendix C: MATLAB Code for Detecting the Best Node to Measure Antiresonance.

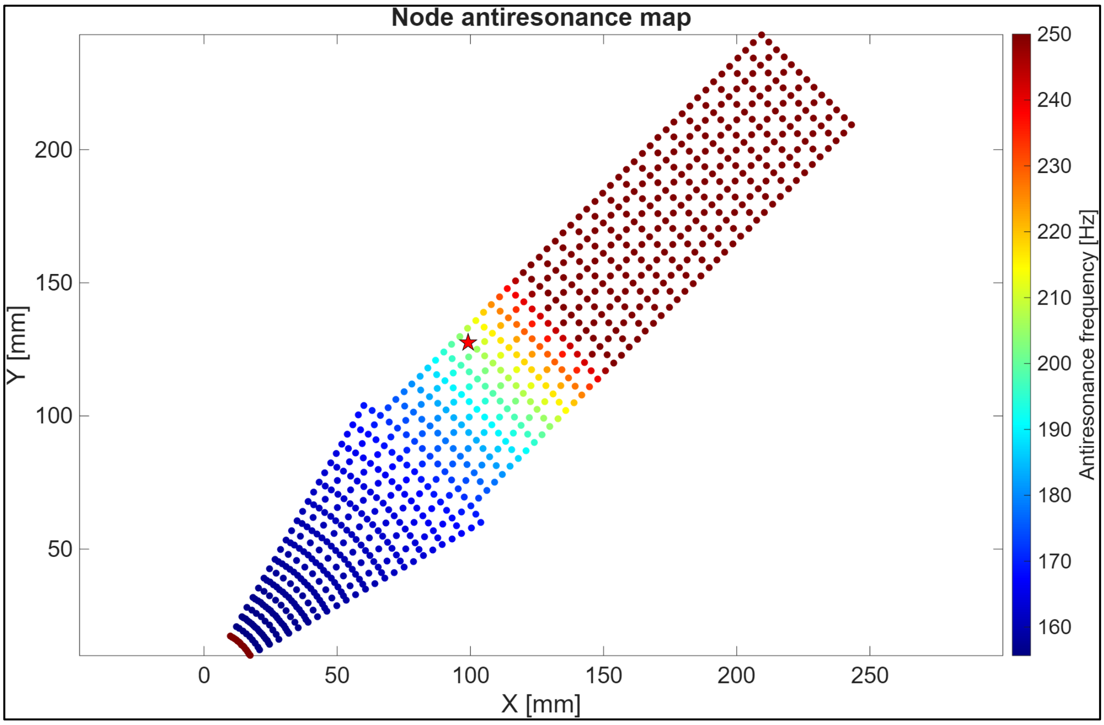

Figure 36 Antiresonance values of the selected nodes

Figure 36 presents the spatial distribution of antiresonance frequencies over the upper surface of the test sector. The color scale encodes the antiresonance frequency identified at each node, ranging approximately 160 Hz at the blade root to over 250 Hz toward the tip. The node whose antiresonance frequency comes closest to the nominal blade-alone frequency is marked with a star.

Since the mistuning introduced by changing elastic moduli is fairly small, the structure behaves consistently, and the mode shapes do not change dramatically from blade to blade. Therefore, the selected point for the measurement can be used repeatedly for the other blades without causing significant errors. Using a single, fixed measurement node across all blade-by-blade tests therefore introduces a negligible additional error while ensuring consistency of the identification method.

4.5. Blade-by-Blade Frequency Comparison

With the optimal measurement node fixed by the MPC strategy, the blade-by-blade detuning procedure of Section 3.4 is applied. For each blade, $n = 1,2, \dots 12$, the detuning masses are relocated so that only blade n is unloaded, the harmonic excitation is applied near its root, and the FRF is computed at the measurement node of the corresponding sector. The deepest minimum in the band [150,220] Hz is recorded as the identified antiresonance frequency $f_i^{a(n)}$. Figure 37 compares three sets of natural frequencies extracted for each of the twelve blades of the blisk: the blade-alone frequency, the antiresonance frequency, and the sector natural frequency. The blade-alone and antiresonance curves nearly coincide across all blades, with the antiresonance frequency consistently underestimating the corresponding blade-alone value by less than 0.6 Hz. This close agreement confirms that the antiresonance frequencies faithfully track the blade-alone frequencies and therefore reproduce the same blade-to-blade scatter, which constitutes the mistuning pattern of the assembly. These findings support the use of antiresonance frequencies as observable substitutes for blade-alone frequencies within the proposed identification strategy. In contrast, the sector frequencies lie substantially lower, between 137.7 Hz and 139.11 Hz, reflecting the coupled dynamic behavior of the full sector rather than the isolated blade. Although the sector frequencies exhibit a comparable scatter trend across the blades, their notably different magnitude shows that inter-blade and disk coupling shift the resonant response of the assembly well below the blade-alone range.

The deviation between blade-alone frequencies and antiresonance frequencies are summarized in Table 6.

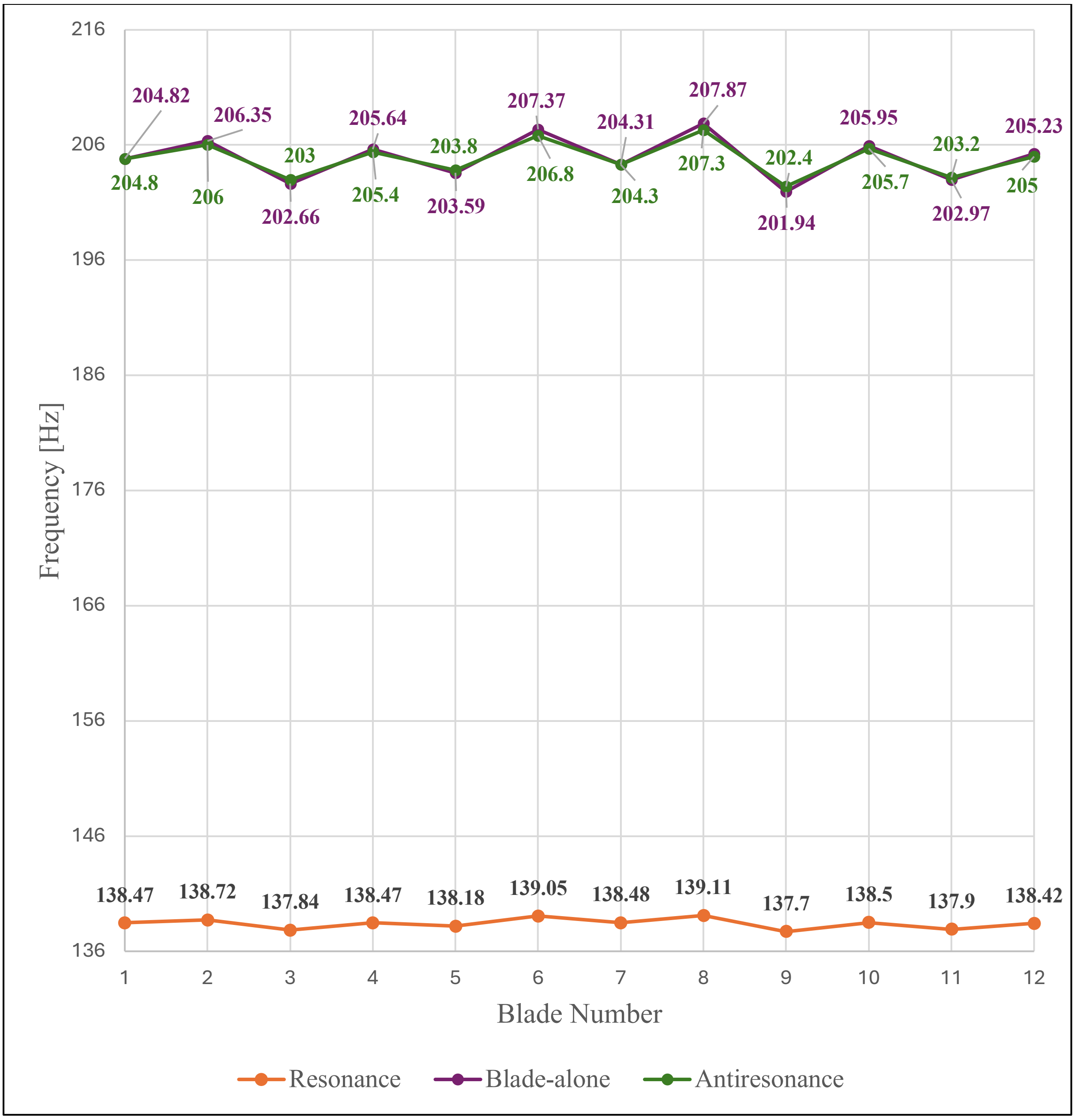

Figure 37 Comparison of blade-alone, antiresonance and resonance frequencies

Table 6 Comparison of natural and antiresonance frequencies for blades 1–12

Blades	Blade-alone Freq. [Hz]	Antiresonance Freq. [Hz]	Difference [%]
Blade 1	204.82	204.8	**-0.01**
Blade 2	206.35	206	**-0.17**
Blade 3	202.66	203	**0.17**
Blade 4	205.64	205.4	**-0.12**
Blade 5	203.59	203.8	**0.10**
Blade 6	207.37	206.8	**-0.27**
Blade 7	204.31	204.3	**0.00**
Blade 8	207.87	207.3	**-0.27**
Blade 9	201.94	202.4	**0.23**
Blade 10	205.95	205.7	**-0.12**
Blade 11	202.97	203.2	**0.11**
Blade 12	205.23	205	**-0.11**

4.6. Identified Young's Modulus Mistuning Pattern

In this step of the validation, the identified antiresonance frequencies of Section 4.5 will be converted into a Young's modulus mistuning pattern and compares it directly with the ground truth imposed in Table 2.

The conversion follows the relationships derived in Section 3.5. For each blade, the frequency mistuning is first calculated from the identified antiresonance frequency f_i^a relative to the nominal reference frequency f_{ref} according to Equation (3.23). The reference is taken as the blade-alone frequency of the nominal blade obtained from the modal analysis explained in Section 4.2 ($f_{ref} = 204.82\ Hz.$) . The frequency mistuning is then mapped to the Young's modulus mistuning through Equation (3.26), $\delta_i^E = \left(1 + \delta_i^f\right)^2 - 1$, and finally to the absolute modulus by using Equation (3.27). To obtain more accurate results, the linear approximation will not be used.

An example of calculations followed for blade 3:

$$\delta_3^f = \frac{f_3^a - f_{ref}}{f_{ref}} = \frac{203 - 204.82}{204.82} = -0.00889 \tag{4.1}$$

From Equation (3.26) and (3.27)

$$\delta_3^E = \left(1 + \delta_3^f\right)^2 - 1 = -0.0177 \tag{4.2}$$

$$E_3 = (1 + \delta_3^E)E_0 = 196.46\ GPa \tag{4.3}$$

The results of this conversion are reported in Table 7, where the identified Young's modulus mistuning of each blade is placed alongside the imposed value of Table 2. The deviation is expressed as percentage.

Table 7 Comparison of introduced and identified Young's modulus for the dummy blisk

Blades	Imposed Young's modulus [GPa]	Identified Young's modulus [GPa]	Deviation [%]
Blade 1	200	199.96	-0.02
Blade 2	203	202.31	-0.34
Blade 3	195.8	196.46	0.34
Blade 4	201.6	201.13	-0.23
Blade 5	197.6	198.01	0.21
Blade 6	205	203.89	-0.54
Blade 7	199	198.99	-0.01
Blade 8	206	204.87	-0.55
Blade 9	194.4	195.30	0.46
Blade 10	202.2	201.72	-0.24
Blade 11	196.4	196.85	0.23
Blade 12	200.8	200.35	-0.22

Overall, the results in Table 7 confirm the validity of the proposed method. The identified Young's modulus values follow the real imposed pattern closely, and the ranking of the blades from least to most mistuned is accurately preserved. While the errors tend to slightly grow with the magnitude of mistuning, the largest absolute deviation is only 0.55% on Blade 8, and all blades exhibit errors well below 1%. This demonstrates that the method can recover the blisk mistuning pattern with excellent accuracy, making it highly suitable for updating the FE model and predicting the forced response.

4.7. Comparison with the Resonance Method

The two identified mistuning parameters, obtained using the antiresonance and resonance methods, will be applied to the blisk model and compared with each other and with the tuned and real mistuned models in this section.

4.7.1. Application of Resonance Method

To determine the reference resonance frequency of the tuned case for the resonance method, the tuned model with detuning masses is used. The same setup shown in Figure 34 is used again, only with the nominal elastic modulus value of the blades. The first bending resonance frequency of the isolated blade is taken as the reference frequency, which is computed as 138.38 Hertz. Then the same detuned model is used for the real mistuned blisk, and a blade-by-blade test is performed on all blades to determine the corresponding resonant frequencies. One example for Blade 3 is shown in Figure 39 with a resonance frequency of 137.84 Hertz. The resulting value is also checked with a harmonic analysis. The modified version of Equation (3.23) is then used to determine the frequency deviation. By using the determined frequency deviation, the Young's modulus of the blades is constructed with Equation (4.5).

$$\delta_i^f = \frac{f_i^{resonance} - f_{ref}^{resonance}}{f_{ref}^{resonance}} \tag{4.4}$$

$$E_i = E_0\left(1 + \delta_i^f\right)^2 \tag{4.5}$$

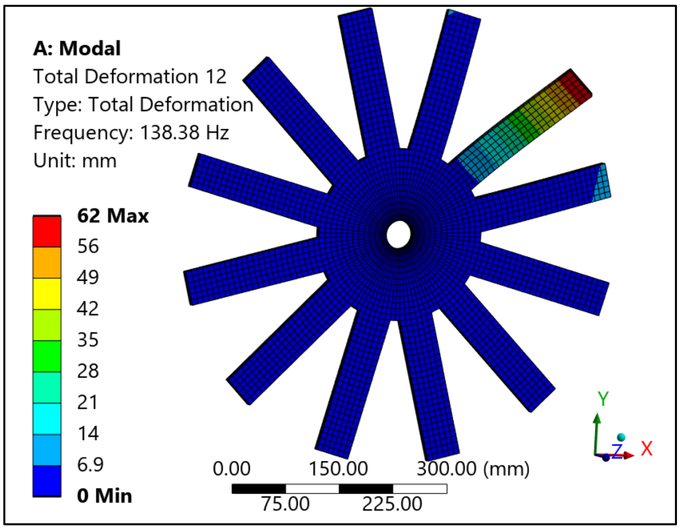

Figure 38 Blade-alone frequency of Blade 1 of the tuned blisk with detuning masses

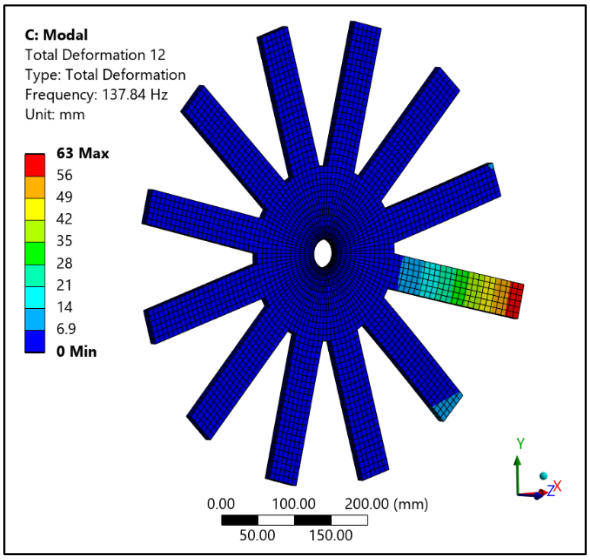

Figure 39 Blade-alone frequency of Blade 3 of the mistuned blisk with detuning masses

Table 8 Values of the resonance method

Blades	Resonance frequency [Hz]	Identified Young's Modulus [GPa]
Nominal Blade	**138.38**	**200**
Blade 1	138.47	200.26
Blade 2	138.72	200.98
Blade 3	137.84	198.44
Blade 4	138.47	200.26
Blade 5	138.18	199.42
Blade 6	139.05	201.94
Blade 7	138.48	200.29
Blade 8	139.11	202.12
Blade 9	137.7	198.04
Blade 10	138.5	200.35
Blade 11	137.9	198.61
Blade 12	138.42	200.12

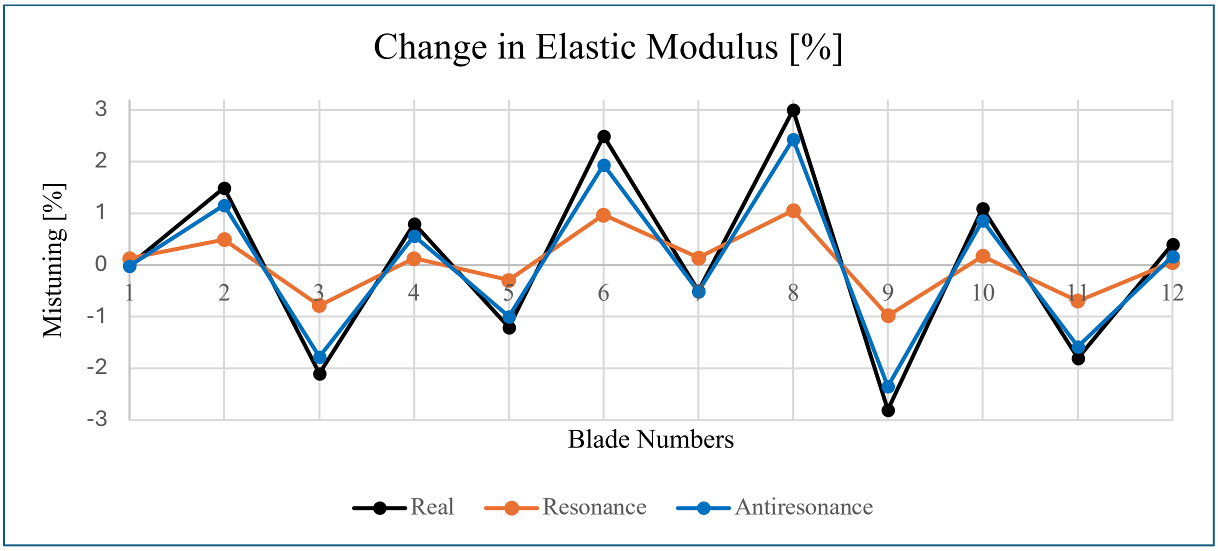

Figure 40 Comparison of mistuning values

Figure 40 shows the mistuning values identified by the resonance and antiresonance method with the real mistuning imposed for this study. Both methods underpredict mistuning value, however resonance method is much closer to a tuned model which has zero mistuning. The identified Young's moduli shown in Table 8 of the blades are then imported into the FE model for the later analyses.

4.7.2. Free Vibration Response Comparison

The modal shapes of the two mistuned models with values identified via the antiresonance and the resonance method are compared with the reference mistuned model in this section. For the comparison, the Modal Assurance Criterion (MAC) ([36]) is used, since it leads to better understanding of the compliance of the mode shapes of different models. MAC uses modal vectors to calculate the coherency of the mode shapes. The mathematical description of MAC matrix is as follows:

$$\mathbf{MAC}_{\text{antires,real}}(i,j) = \frac{\left|\boldsymbol{\phi}_{antires,i}^{T}\boldsymbol{\phi}_{real,j}\right|^{2}}{\left(\boldsymbol{\phi}_{antires,i}^{T}\boldsymbol{\phi}_{antires,i}\right)\left(\boldsymbol{\phi}_{real,j}^{T}\boldsymbol{\phi}_{real,j}\right)} \tag{4.6}$$

$$\mathbf{MAC}_{\text{res,real}}(i,j) = \frac{\left|\boldsymbol{\phi}_{res,i}^{T}\boldsymbol{\phi}_{real,j}\right|^{2}}{\left(\boldsymbol{\phi}_{res,i}^{T}\boldsymbol{\phi}_{res,i}\right)\left(\boldsymbol{\phi}_{real,j}^{T}\boldsymbol{\phi}_{real,j}\right)} \tag{4.7}$$

Where $\boldsymbol{\phi}_{antires,i}$ and $\boldsymbol{\phi}_{res,i}$ are the eigenvectors of mode shape i of the antiresonance-based mistuned model, and resonance-based mistuned model, respectively. $\boldsymbol{\phi}_{real,j}$ is the eigenvector of mode shape j of the real mistuned model. A MAC score approaching unity (1.0) reflects a robust linear relationship between the compared mode shapes, thereby validating the precision and reliability of the modal extraction process. For this analysis, one node from each blade tip is selected to create modal displacement vectors. Then the collected data is processed by using the code given in Appendix D: MATLAB Code to Process MAC Data. By using the code, Figure 41 is constructed to illustrate the correlation of the mode shapes.

The first 12 modes are compared, and their frequencies can be seen in Table 9. The MAC matrices comparing the real mistuning with the identified mistuning for both the antiresonance and resonance methods can be seen in Figure 41. Because both methods give highly accurate results, the standard linear matrices were almost perfectly diagonal. Therefore, a logarithmic scale is used to exaggerate the off-diagonal terms so the underlying errors could be analyzed. Even under this exaggerated scale, the antiresonance method maintains a very clean profile, showing its precision. Only for the first two modes, which have nodal diameter 1, the antiresonance-based mistuned model gives inferior results than the resonance-based method. On the other hand, the resonance method shows some visible errors off- diagonal, especially in the higher index range between 8 and 12.

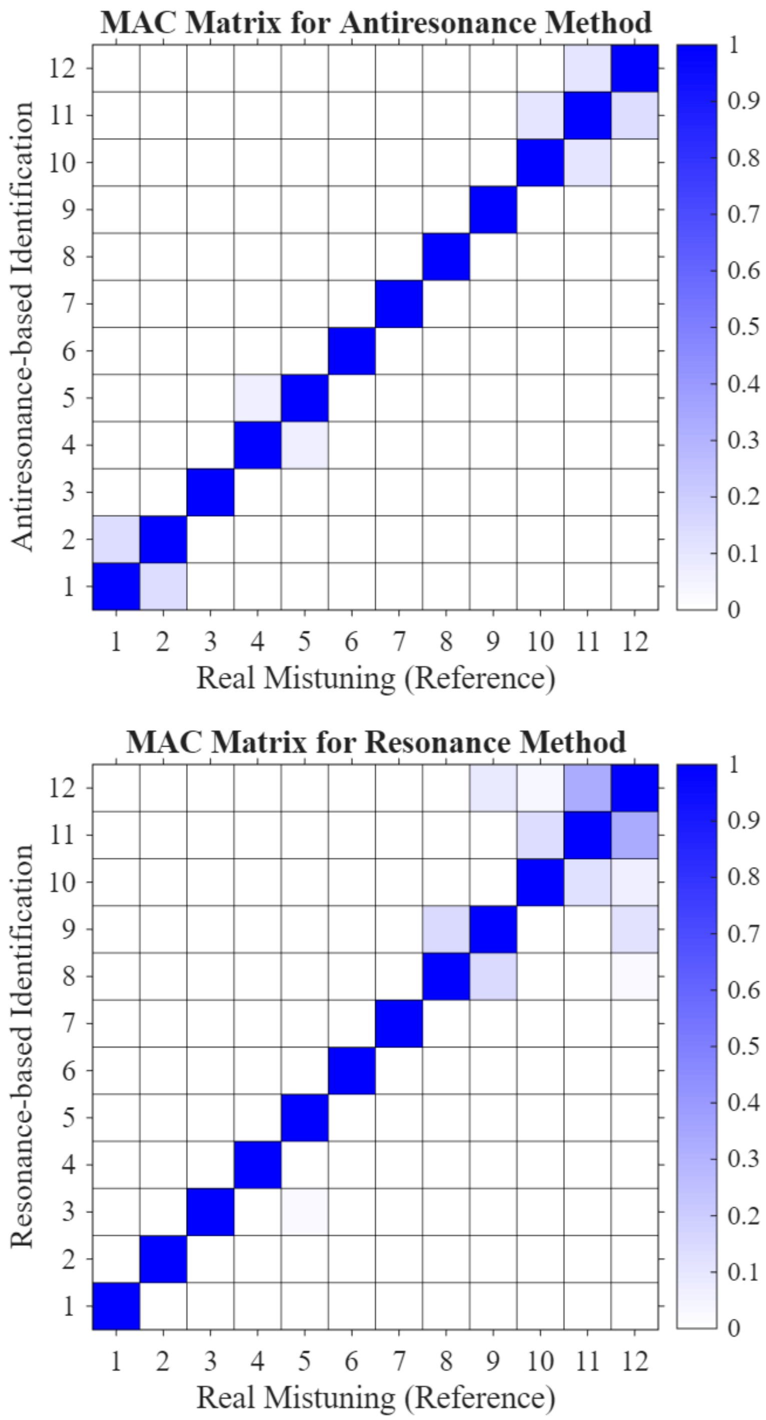

Figure 41 MAC matrices for both methods

4.7.3. Engine Order Excitation Response Comparison

The comparison of the mentioned identification methods will be done by using the amplification factors (AF) defined by the following formula.

$$\boldsymbol{AF} = \frac{\text{Maximum amplitude of } \textbf{mistuned} \text{ blisk under EO excitation}}{\text{Maximum amplitude of } \textbf{tuned} \text{ blisk under EO excitation}} \tag{4.8}$$

To compare the methods, four different blisk models will be used. These are:

1. Tuned (nominal) blisk
2. Real mistuned blisk
3. Mistuned blisk with values identified via the antiresonance method
4. Mistuned blisk with values identified via the resonance method

The natural frequencies of the first model, tuned blisk, have been already calculated and showed in Figure 27. These frequencies are used to calculate the maximum response of the tuned model with engine order excitation. To find the frequency of the nodal diameters of the mistuned models, first a modal analysis is performed. The result of the real mistuned blisk is shown in the following table as an example.

Table 9 Modes and frequencies of the real mistuned blisk

Nodal Diameter	Mode	Frequency [Hz]
1	1	97.758
1	2	97.85
0	3	107.6
2	4	111.27
2	5	111.37
3	6	141.55
3	7	142.61
4	8	157.32
4	9	157.61
5	10	164.18
5	11	164.67
6	12	166.5
0	13	402.97
1	14	531.06

In the first two modes of this model nodal diameter is 1. Mode 3 is the mode shape with nodal diameter 0 (umbrella mode). This can be better understood by looking at the Figure 27. From this table, the frequency range of different nodal diameters can be properly defined to find the amplitude of the deflection. Until this point, the modal analyses are performed to determine the frequency range to use for different engine order excitations of different models.

The same engine order excitation simulation is performed for all four models. A named selection is created in ANSYS to define the surfaces where the forces are applied. Figure 42 illustrates these surfaces, which correspond to the blade tips. Then 12 forces on the axial (Z) direction are introduced to each selection. The engine order is defined by adjusting the "Z Phase Angle" in ANSYS, according to formulation explained by Equation (1.27). The total deformation of these surfaces is then evaluated using the frequency values listed in Table 9. Generally, the response amplitude exhibits a peak between the split frequencies of the corresponding nodal diameter mode shape. As an example, the frequency response of the engine order 4 excitation case for the real mistuned blisk is shown in Figure 44. The peak of this response occurs at 157.58 Hz which falls between 157.32 and 157.61 Hz, the frequencies of mode 8 and 9, respectively (see Table 9). Therefore, the amplitude at 157.58 Hz is extracted as the maximum amplitude for this configuration.

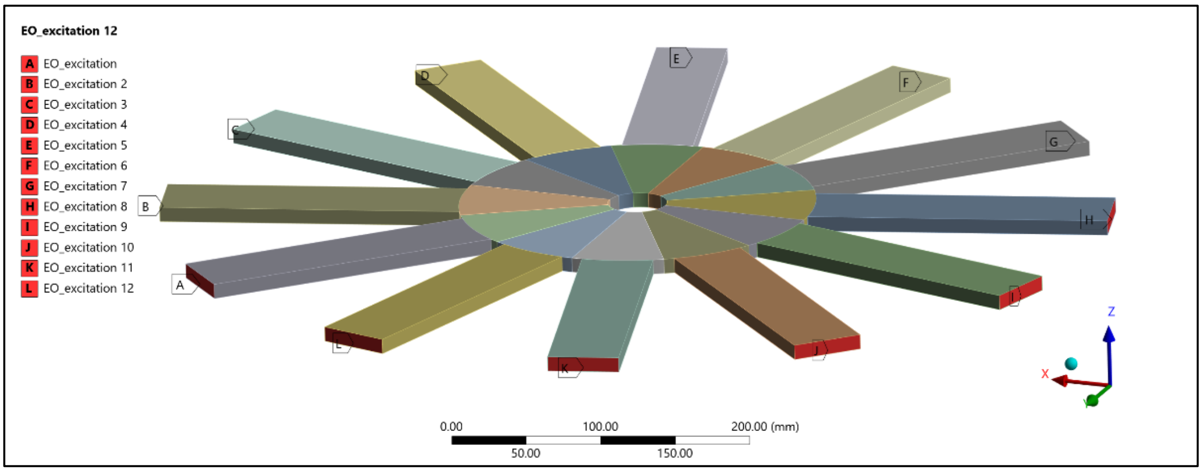

Figure 42 The selected excitation surfaces

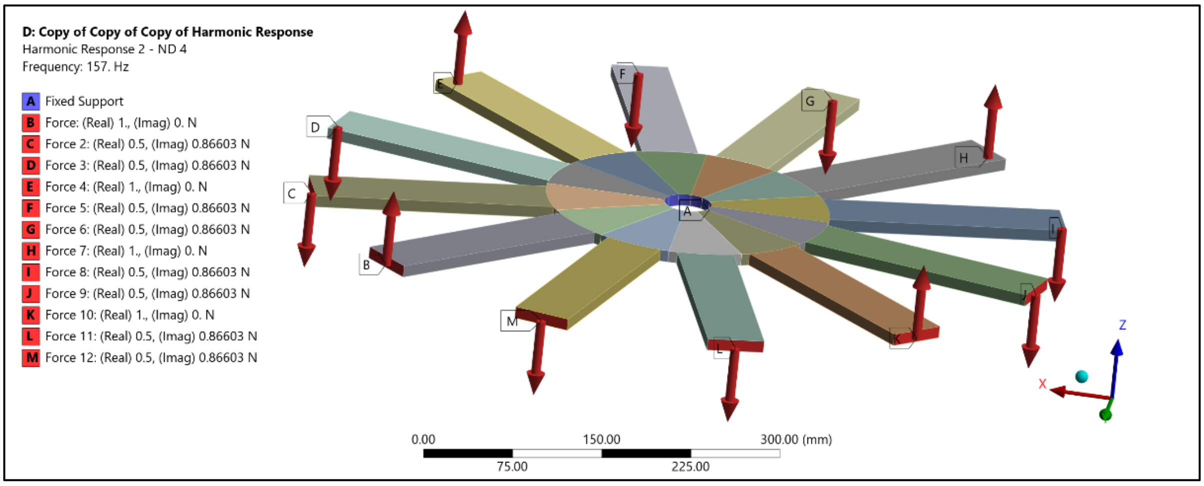

Figure 43 Engine order forces on the tip of the blades

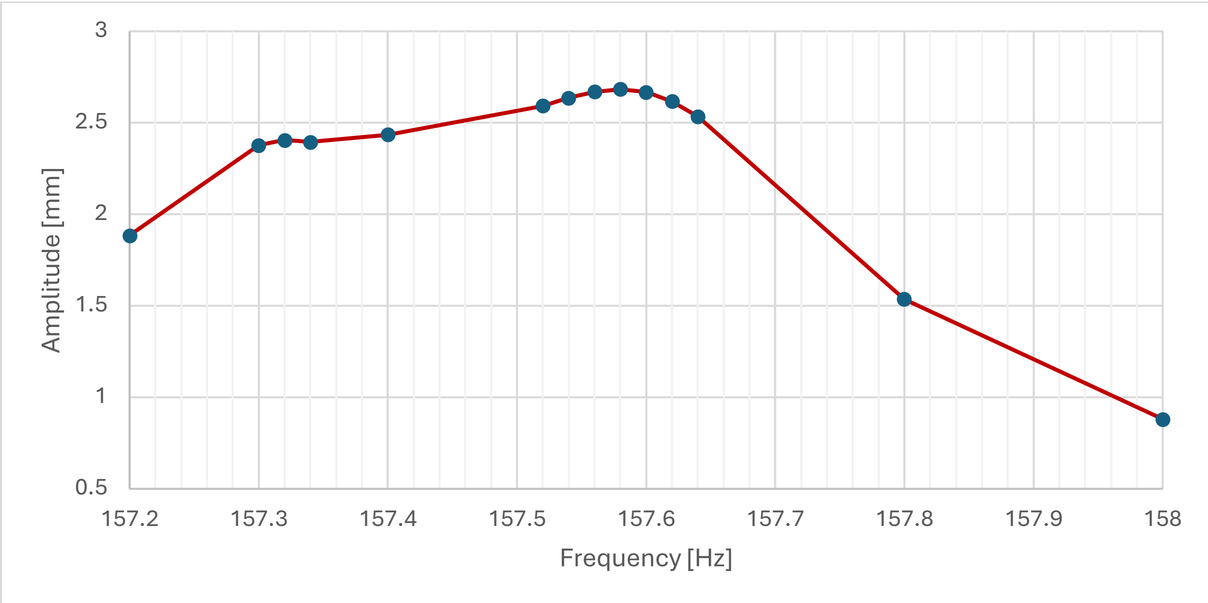

Figure 44 Frequency response of real mistuned blisk excited with engine order 4

Equation (4.8) is used to test the models for 4 different engine order excitations exciting 4 different nodal diameters. The comparison of the 3 different mistuned models can be seen in Figure 45. The antiresonance based mistuned model follows the real mistuned model closely, while the resonance method only gives a comparable result for nodal diameter 3.

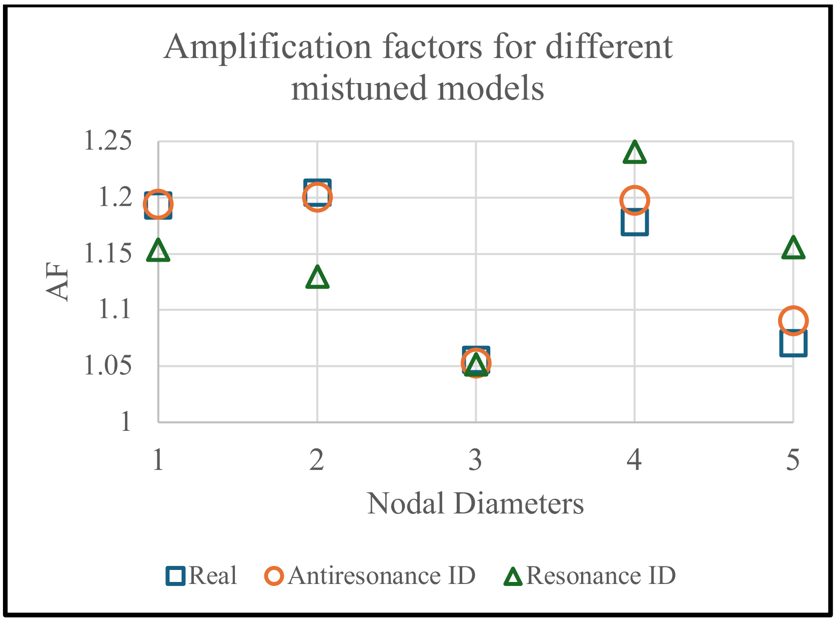

Figure 45 AF of three mistuned models

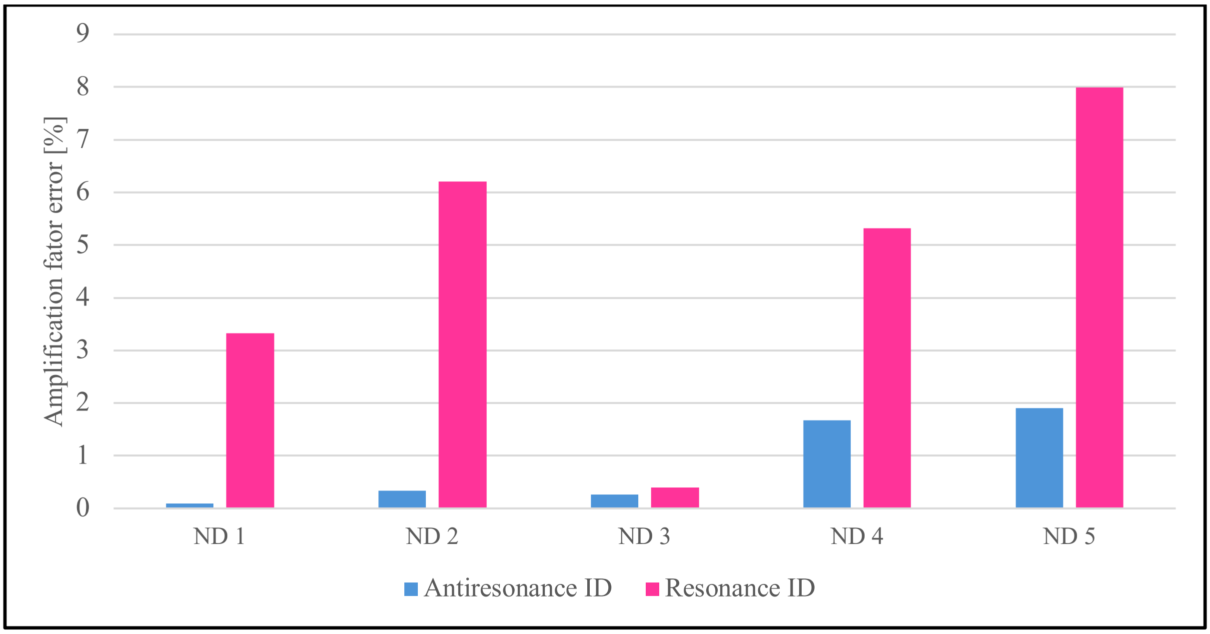

Figure 46 Errors based on real mistuning

The errors of two identified mistuned models based on the real mistuned model can be seen in Figure 46. Even though the mesh used for this analysis is on the coarse side, the errors of the antiresonance method stay under 2%. It can be therefore assumed that it is possible to have even more accurate results with a finer mesh. On the other hand, the resonance method only gives accurate results for the nodal diameter 3, for the other simulations its error is more than 3% reaching up to 8%.

5. Conclusion

A novel antiresonance-based mistuning identification method for integrally bladed disks is validated in this master thesis. The motivation is the blade-disk coupling provided by the shared disk, which prevents any blade from being measured in true isolation and limits the accuracy of conventional resonance-based identification. By treating the blisk as a cyclic metamaterial with blades as local resonators, the method maps the blade-alone frequency of every sector to an antiresonance obtained from frequency response function at a point along the blade. A Measurement Point Correction (MPC) strategy was introduced to recover the true blade-alone frequency from a single measurement node, selected as the location whose antiresonance frequency coincides with the reference value.

The method was validated on a twelve-bladed dummy blisk built in ANSYS Mechanical, in which the mistuning was imposed only by differentiating the Young's modulus of the blades. Because the imposed pattern is known exactly, the ground truth was available without any doubt. The MPC strategy is applied once on the tuned model to fix the measurement node, and the blade-by-blade detuning procedure, using point masses of 0.5 kg on every blade except the one under test, is then applied to the mistuned model to isolate a single antiresonance for each sector.

The identified antiresonance frequencies reproduce the blade-alone frequencies closely, with a frequency deviation below 0.3% across all twelve blades and the blade-to-blade scatter of the mistuning pattern preserved. The identified Young's modulus deviates from the imposed value by at most 0.55% on the most mistuned blade, while most blades remain below 0.35%. This is because the Young’s modulus scales with the square of the frequency. The ranking of the blades from least to most mistuned is retained, which confirms that the identified pattern can be inserted into the finite element model to update the blade elastic properties and to predict the forced response. On this basis the method recovers blade-alone frequencies on a monolithic blisk, where the broach-block test used for inserted-blade disks cannot be applied.

In the last part of this study, the main method examined in this thesis is compared with the previously used resonance-based method. The mistuned models constructed by using the values coming from the two identification methods and then their free vibration response and engine order excitation response are inspected. The antiresonance-based method shows superior accuracy especially for the forced response. The accuracy of the resonance-based method is worsened as the nodal diameter of the mode shapes increased.

Certain simplifications are made during the validation part of this thesis. The study is entirely numerical, and experimental confirmation is still required. An experimental validation is required because the MPC strategy is ultimately motivated by sensor placement in a physical test. The dummy blisk is a deliberately simplified planar model without blade twist, airfoil shape, and root fillet. Also, the mistuning is restricted to the stiffness of the blades, with mass and geometry held at their nominal values. Besides, the analysis is stationary, so it neglects the centrifugal stiffening and Coriolis effects that act at operating speed.

These limitations define the natural directions for future work. The most obvious one is an experimental validation on a manufactured blisk, which would confirm the practical benefit of the MPC strategy. The method should then be extended to rotating conditions, so that the centrifugal and Coriolis effects highlighted in the literature part are captured and applied to a realistic blade geometry with twist and an airfoil section. Treating combined stiffness, mass, and geometric mistuning, and quantifying the residual coupling left after detuning, would further close the gap between the controlled numerical model and a real component. The accuracy of the present results can also be improved within the existing framework by refining the mesh and reducing the frequency step of the harmonic analysis.

Appendix A: Automation Code for Extraction of Frequency Response of the Selected Nodes

```
import os
from Ansys.Mechanical.DataModel.Enums import NormalOrientationType
# --- 1. SETTINGS ---
ns_name = "FRF_nodes"
output_folder = r"C:\Users\pc2\OneDrive\Desktop\forced
response\FRF_data_final"

if not os.path.exists(output_folder):
    os.makedirs(output_folder)

analysis = Model.Analyses[0]
solution = analysis.Solution
ns = DataModel.GetObjectsByName(ns_name)

if not ns:
    print("Error: Named Selection not found. Check spelling.")
else:
    ns = ns[0]
    node_ids = ns.Location.Ids
    print("Starting FRF export for {} nodes...".format(len(node_ids)))

    # Gain access to the Tabular Data window in the UI
    pane = ExtAPI.UserInterface.GetPane(MechanicalPanelEnum.TabularData)

    # --- 3. LOOP AND EXTRACT DATA ---
    for nid in node_ids:

        node_sel =
ExtAPI.SelectionManager.CreateSelectionInfo(SelectionTypeEnum.MeshNodes)
        node_sel.Ids = [nid]

        frf = solution.AddDeformationFrequencyResponse()
        frf.NormalOrientation = NormalOrientationType.ZAxis
        frf.Location = node_sel
        frf.EvaluateAllResults()

        # 'Activate' clicks the object in the tree so the Tabular Data
window updates
        frf.Activate()
        table = pane.ControlUnknown

        file_path = os.path.join(output_folder, "Node_" + str(nid) +
"_FRF.txt")

        # Read the table and write it to our text file line-by-line
```

```python
with open(file_path, "w") as f:
    f.write("Frequency(Hz)\tAmplitude\tPhase\n")

    # Row 1 is headers, so data starts at Row 2
    for row in range(2, table.RowsCount + 1):
        try:
            freq = table.cell(row, 2).Text
            amp = table.cell(row, 3).Text
            phase = table.cell(row, 4).Text
            f.write(freq + "\t" + amp + "\t" + phase + "\n")
        except:
            pass # Skips empty/invalid rows safely

frf.Delete()
```

Appendix B: Python Code to Determine the Antiresonance Frequency of the Selected Nodes

```python
import pandas as pd
import numpy as np
import glob
import os

def process_frf_files(input_directory, output_excel_path):
    results = []

    file_pattern = os.path.join(input_directory, '*.txt')
    file_list = glob.glob(file_pattern)

    print(f"Found {len(file_list)} files to process...")

    for file_path in file_list:
        filename = os.path.basename(file_path)

        try:
            node_id = filename.split('_')[1]
        except IndexError:
            node_id = filename

        try:
            df = pd.read_csv(file_path, sep='\t', decimal=',')
            df.columns = df.columns.str.strip()

            # Replace any 0 or negative amplitudes with a tiny number (1e-
20)
            # This prevents the "divide by zero" log10 error while keeping
it the minimum value
            safe_amplitude = np.where(df['Amplitude'] <= 0, 1e-20,
df['Amplitude'])
            df['Amplitude_dB'] = 20 * np.log10(safe_amplitude)

            # Find the global minimum amplitude in dB
            min_idx = df['Amplitude_dB'].idxmin()

            # Get the corresponding frequency
            min_freq = df.loc[min_idx, 'Frequency(Hz)']

            # Condition: If > 100 Hz, record it. If <= 100 Hz, record 250.
            if min_freq > 100:
                recorded_freq = min_freq
            else:
                recorded_freq = 250

            results.append({
```

```
                'Node': node_id,
                'Original_Min_Freq_Hz': min_freq,
                'Recorded_Frequency': recorded_freq
            })

        except Exception as e:
            print(f"Error processing file {filename}: {e}")

    # Save the consolidated results
    results_df = pd.DataFrame(results)
    results_df.to_csv(output_excel_path, index=False)
    print(f"Processing complete! Results saved to {output_excel_path}")

# --- How to run ---
input_folder = '.'
output_file = 'Processed_Nodes_Results.csv'

process_frf_files(input_folder, output_file)
```

Appendix C: MATLAB Code for Detecting the Best Node to Measure Antiresonance

```
%% ============================================================
%  Antiresonance node map  (MATLAB)
%  Scatter of nodes on the X-Y plane, colored by antiresonance
%  frequency, with a star marking the reference node (the one
%  whose antiresonance is closest to the blade-alone frequency).
%  ============================================================

%% --- settings ----------------------------------------------
csvPath    = 'Antiresonances.csv';
bladeAlone = 204.82;        % blade-alone reference frequency [Hz]

%% --- load data ---------------------------------------------
T = readtable(csvPath);

X = T.X * 1000;             % m -> mm
Y = T.Y * 1000;

F = T.Recorded_Frequency;

%% --- pick the star node (closest to blade-alone frequency) ----
[~, iStar] = min(abs(F - bladeAlone));

%% --- plot --------------------------------------------------
figure('Color','w');

scatter(X, Y, 36, F, 'filled');          % nodes colored by frequency
hold on;
plot(X(iStar), Y(iStar), 'rp', ...       % red pentagram (star)
     'MarkerSize', 16, ...
     'MarkerFaceColor', 'r', ...
     'MarkerEdgeColor', 'k');

colormap(jet);  %color map according to distance from blade-alone frequency
cb = colorbar;
cb.Label.String = 'Antiresonance frequency [Hz]';

axis equal;
xlabel('X [mm]');
ylabel('Y [mm]');
title('Node antiresonance map');
box on;
set(gca, 'FontSize', 20);
```

Appendix D: MATLAB Code to Process MAC Data

```
%% Clear environment
clc; clear; close all;

%% 1. Load and Format Data
% Load mode shapes from .mat files
data_real = load("modes_real.mat");
data_antires = load("modes_antiresID.mat");
data_res = load("modes_resID.mat");

% Extract the 12 cells into 36x12 matrices
% Using cat(2, ...) horizontally concatenates the column vectors inside the cells
phi_real = cat(2, data_real.mode_real{:});
phi_antires = cat(2, data_antires.mode_antiresID{:});
phi_res = cat(2, data_res.mode_resID{:});

%% 2. Calculate and Plot MAC Matrices

% Top plot: Antiresonance-based Identification
subplot(2, 1, 1);
plot_mac(phi_real, phi_antires, ...
    'Antiresonance-based Identification', ...
    'MAC Matrix for Antiresonance Method');

% Bottom plot: Resonance-based Identification
subplot(2, 1, 2);
plot_mac(phi_real, phi_res, ...
    'Resonance-based Identification', ...
    'MAC Matrix for Resonance Method');

%% ------------------------------------------------------------------------
%% Local Functions
%% ------------------------------------------------------------------------

function plot_mac(phi_ref, phi_test, y_label, plot_title)
    % 1. Calculate the MAC Matrix (12x12)
    cross_prod = (phi_ref' * phi_test).^2;
    auto_ref = diag(phi_ref' * phi_ref);
    auto_test = diag(phi_test' * phi_test);
    MAC_matrix = cross_prod ./ (auto_ref * auto_test');

    % 2. Plot Logarithmic MAC (draws into the current active subplot)
    MAC_log = log10(MAC_matrix + eps);
    MAC_log = (MAC_log + 4) / 4; % Scales [-4, 0] to [0, 1]
    imagesc(MAC_log);

    % 3. Apply Custom White-to-Blue Colormap
    % Define start (White) and end (Dark Blue) colors in RGB
    color_start = [1, 1, 1];       % White
    color_end   = [0, 0, 1];    % Dark Blue

    % Interpolate to create 100 color steps
    n_colors = 100;
    cmap = [linspace(color_start(1), color_end(1), n_colors)', ...
            linspace(color_start(2), color_end(2), n_colors)', ...
            linspace(color_start(3), color_end(3), n_colors)'];
```

```
    colormap(gca, cmap);

    colorbar;
    caxis([0 1]);

    % 4. Format the axes
    set(gca, 'YDir', 'normal', 'TickDir', 'out', 'Box', 'on');
    xticks(1:12);
    yticks(1:12);
    xlabel('Real Mistuning (Reference)');
    ylabel(y_label);
    title(plot_title, 'FontWeight', 'bold');

    % 5. Draw the grid lines to make the boxes
    hold on;
    for i = 0.5:1:12.5
        xline(i, 'k-', 'LineWidth', 0.5);
        yline(i, 'k-', 'LineWidth', 0.5);
    end
    hold off;

    % Force the plot to be perfectly square
    axis square;
end
```

References

[1] S. Zucca and T. Berruti, “Dynamics of bladed discs Mistuning”.
[2] M. P. Castanier and C. Pierre, “Modeling and Analysis of Mistuned Bladed Disk Vibration: Current Status and Emerging Directions,” *J. Propuls. Power*, vol. 22, no. 2, pp. 384–396, Mar. 2006, doi: 10.2514/1.16345.
[3] R. Bladh, M. P. Castanier, and C. Pierre, “Component-Mode-Based Reduced Order Modeling Techniques for Mistuned Bladed Disks—Part I: Theoretical Models,” *J. Eng. Gas Turbines Power*, vol. 123, no. 1, pp. 89–99, Apr. 2000, doi: 10.1115/1.1338947.
[4] M. P. Castanier, G. Óttarsson, and C. Pierre, “A Reduced Order Modeling Technique for Mistuned Bladed Disks,” *J. Vib. Acoust.*, vol. 119, no. 3, pp. 439–447, Jul. 1997, doi: 10.1115/1.2889743.
[5] M.-T. Yang and J. H. Griffin, “A Reduced Order Approach for the Vibration of Mistuned Bladed Disk Assemblies,” *J. Eng. Gas Turbines Power*, vol. 119, no. 1, pp. 161–167, Jan. 1997, doi: 10.1115/1.2815542.
[6] R. R. Craig and M. C. C. Bampton, “Coupling of substructures for dynamic analyses.,” *AIAA J.*, vol. 6, no. 7, pp. 1313–1319, Jul. 1968, doi: 10.2514/3.4741.
[7] S.-H. Lim, R. Bladh, M. P. Castanier, and C. Pierre, “Compact, Generalized Component Mode Mistuning Representation for Modeling Bladed Disk Vibration,” *AIAA J.*, vol. 45, no. 9, pp. 2285–2298, Sep. 2007, doi: 10.2514/1.13172.
[8] M.-T. Yang and J. H. Griffin, “A Reduced-Order Model of Mistuning Using a Subset of Nominal System Modes,” *J. Eng. Gas Turbines Power*, vol. 123, no. 4, pp. 893–900, Oct. 2001, doi: 10.1115/1.1385197.
[9] D. M. Feiner and J. H. Griffin, “A Fundamental Model of Mistuning for a Single Family of Modes,” *J. Turbomach.*, vol. 124, no. 4, pp. 597–605, Nov. 2002, doi: 10.1115/1.1508384.
[10] P. Vargiu, C. M. Firrone, S. Zucca, and M. M. Gola, “A reduced order model based on sector mistuning for the dynamic analysis of mistuned bladed disks,” *Int. J. Mech. Sci.*, vol. 53, no. 8, pp. 639–646, Aug. 2011, doi: 10.1016/j.ijmecsci.2011.05.010.
[11] E. P. Petrov, K. Y. Sanliturk, and D. J. Ewins, “A New Method for Dynamic Analysis of Mistuned Bladed Disks Based on the Exact Relationship Between Tuned and Mistuned Systems,” *J. Eng. Gas Turbines Power*, vol. 124, no. 3, pp. 586–597, Jul. 2002, doi: 10.1115/1.1451753.
[12] S. Willeke, L. Panning-Von Scheidt, and J. Wallaschek, “Reduced Order Modeling of Mistuned Bladed Disks under Rotation,” *Tech. Mech. 37 2-5 314-325 ISSN 2199-9244*, p. 2,44 MB, 2017, doi: 10.24352/UB.OVGU-2017-107.
[13] D. M. Feiner and J. H. Griffin, “Mistuning Identification of Bladed Disks Using a Fundamental Mistuning Model—Part I: Theory,” *J. Turbomach.*, vol. 126, no. 1, pp. 150–158, Jan. 2004, doi: 10.1115/1.1643913.
[14] D. M. Feiner and J. H. Griffin, “Mistuning Identification of Bladed Disks Using a Fundamental Mistuning Model: Part 2 — Application,” in *Volume 4: Turbo Expo 2003*, Atlanta, Georgia, USA: ASMEDC, Jan. 2003, pp. 279–286. doi: 10.1115/GT2003-38953.
[15] Y. Bhartiya and A. Sinha, “Geometric Mistuning Identification of Integrally Bladed Rotors Using Modified Modal Domain Analysis,” *J. Eng. Gas Turbines Power*, vol. 136, no. 12, p. 122504, Dec. 2014, doi: 10.1115/1.4027762.
[16] J. A. Beck, J. M. Brown, D. L. Gillaugh, E. B. Carper, and A. A. Kaszynski, “Integrally Bladed Rotor Mistuning Identification and Model Updating Using Geometric Mistuning Models,” *J. Eng. Gas Turbines Power*, vol. 143, no. 12, p. 121012, Dec. 2021, doi: 10.1115/1.4051111.

[17] A. Lupini, J. Shim, S. Callan, and B. I. Epureanu, “Mistuning Identification Technique Based on Blisk Detuning,” *AIAA J.*, vol. 59, no. 8, pp. 3087–3095, Aug. 2021, doi: 10.2514/1.J060209.
[18] M. Cimpuieru, S. T. Kelly, A. Lupini, C. Keener, K. D’Souza, and B. I. Epureanu, “Mistuning Identification of Blisks Using Mass Detuning and Influence Coefficients,” *AIAA J.*, vol. 61, no. 8, pp. 3682–3691, Aug. 2023, doi: 10.2514/1.J062668.
[19] A. Li, W. Wang, Y. Fan, T. M. Berruti, and Y. Wu, “Mistuning Identification of Blisk Based on Antiresonance,” *Mech. Syst. Signal Process.*, vol. 239, p. 113307, Oct. 2025, doi: 10.1016/j.ymssp.2025.113307.
[20] D. Wei, H. Li, P. Gao, Y. Chen, and C. Wang, “Mistuning identification and model updating approach for bladed disks based on blade tip timing,” *J. Sound Vib.*, vol. 567, p. 117958, Dec. 2023, doi: 10.1016/j.jsv.2023.117958.
[21] W. Long and Y. Chen, “Reduced order modeling and mistuning identification method for rotating bladed disks under varying speeds,” *J. Sound Vib.*, vol. 595, p. 118687, Jan. 2025, doi: 10.1016/j.jsv.2024.118687.
[22] D. Liang, J. Yao, Z. Jia, Z. Cao, X. Liu, and X. Jing, “Novel Neural Network for Predicting the Vibration Response of Mistuned Bladed Disks,” *AIAA J.*, vol. 61, no. 1, pp. 391–405, Jan. 2023, doi: 10.2514/1.J062215.
[23] J. Sun and J. Zhou, “Metamaterials: The Art in Materials Science,” *Engineering*, vol. 44, pp. 145–161, Jan. 2025, doi: 10.1016/j.eng.2024.12.011.
[24] P. Jiao, J. Mueller, J. R. Raney, X. (Rayne) Zheng, and A. H. Alavi, “Mechanical metamaterials and beyond,” *Nat. Commun.*, vol. 14, no. 1, p. 6004, Sep. 2023, doi: 10.1038/s41467-023-41679-8.
[25] D. R. Smith and N. Kroll, “Negative Refractive Index in Left-Handed Materials,” *Phys. Rev. Lett.*, vol. 85, no. 14, pp. 2933–2936, Oct. 2000, doi: 10.1103/PhysRevLett.85.2933.
[26] “Experimental Verification of a Negative Index of Refraction.” Accessed: May 15, 2026. [Online]. Available: https://www.science.org/doi/10.1126/science.1058847
[27] X. Xue, C. Lin, F. Wu, Z. Li, and J. Liao, “Lattice structures with negative Poisson’s ratio: A review,” *Mater. Today Commun.*, vol. 34, p. 105132, Mar. 2023, doi: 10.1016/j.mtcomm.2022.105132.
[28] H. Meng, D. Chronopoulos, A. T. Fabro, W. Elmadih, and I. Maskery, “Rainbow metamaterials for broadband multi-frequency vibration attenuation: Numerical analysis and experimental validation,” *J. Sound Vib.*, vol. 465, p. 115005, Jan. 2020, doi: 10.1016/j.jsv.2019.115005.
[29] W. D′Ambrogio and A. Fregolent, “Substructure decoupling without using rotational DoFs: Fact or fiction?,” *Mech. Syst. Signal Process.*, vol. 72–73, pp. 499–512, May 2016, doi: 10.1016/j.ymssp.2015.11.029.
[30] V. Meruane, “Model updating using antiresonant frequencies identified from transmissibility functions,” *J. Sound Vib.*, vol. 332, no. 4, pp. 807–820, Feb. 2013, doi: 10.1016/j.jsv.2012.10.021.
[31] D. J. Mead, “Waves and Modes in Finite Beams: Application of the Phase-Closure Principle,” *J. Sound Vib.*, vol. 171, no. 5, pp. 695–702, Apr. 1994, doi: 10.1006/jsvi.1994.1150.
[32] H. Sun, X. Du, and P. Pai, “Theory of Metamaterial Beams for Broadband Vibration Absorption,” *J. Intell. Mater. Syst. Struct.*, vol. 21, pp. 1085–1101, Jul. 2010, doi: 10.1177/1045389X10375637.
[33] B. Zhou, J. Zhao, and T. M. Berruti, “Exploration of blade detuning tests for mistuning identification of blisks,” *Mech. Syst. Signal Process.*, vol. 175, p. 109118, Aug. 2022, doi: 10.1016/j.ymssp.2022.109118.

[34] D. J. Inman and R. C. Singh, *Engineering vibration*, 4. ed., Internat. ed. in Always Learning. Boston, Mass. München: Pearson, 2014.

[35] B. Zhou, J. Zhao, N. Ye, and T. M. Berruti, “Blisk With Small Geometry Mistuning and Blend Repair: As-Measured Finite Element Model and Experimental Verification,” *J. Eng. Gas Turbines Power*, vol. 144, no. 10, p. 101017, Oct. 2022, doi: 10.1115/1.4055363.

[36] M. Pastor, M. Binda, and T. Harčarik, “Modal Assurance Criterion,” *Procedia Eng.*, vol. 48, pp. 543–548, 2012, doi: 10.1016/j.proeng.2012.09.551.